Opto-Electronic Science

Review

2022, Vol. 1, No. 12

DOI: 10.29026/oes.2022.220020

High-speed visible light communication based on micro-LED: A technology with wide applications in next generation communication

Tingwei Lu[1], Xiangshu Lin[1], Wenan Guo[1], Chang-Ching Tu[3,4], Shibiao Liu[1], Chun-Jung Lin[5], Zhong Chen[1,2], Hao-Chung Kuo[3,4]* and Tingzhu Wu[1,2]*

The evolution of next-generation cellular networks is aimed at creating faster, more reliable solutions. Both the next-generation 6G network and the metaverse require high transmission speeds. Visible light communication (VLC) is deemed an important ancillary technology to wireless communication. It has shown potential for a wide range of applications in next-generation communication. Micro light-emitting diodes (μLEDs) are ideal light sources for high-speed VLC, owing to their high modulation bandwidths. In this review, an overview of μLEDs for VLC is presented. Methods to improve the modulation bandwidth are discussed in terms of epitaxy optimization, crystal orientation, and active region structure. Moreover, electroluminescent white LEDs, photoluminescent white LEDs based on phosphor or quantum-dot color conversion, and μLED-based detectors for VLC are introduced. Finally, the latest high-speed VLC applications and the application prospects of VLC in 6G are introduced, including underwater VLC and artificial intelligence-based VLC systems.

Keywords: visible light communication; μLEDs; modulation bandwidth; detector; 6G

Lu TW, Lin XS, Guo QA, Tu CC, Liu SB et al. High-speed visible light communication based on micro-LED: A technology with wide applications in next generation communication. *Opto-Electron Sci* **1**, 220020 (2022).

Introduction

Innovations in smartphones and smart homes, and the emergence of online services have propelled the growth of cloud computing, the Internet of Things, and autonomous driving[1–6]. In the future, the metaverse, a fledgling networking technology, will allow users to experience multimedia by combining distributed real-time sources and stored digital assets in real time. However, its real-time interactive nature will significantly increase requirements for data storage and transmission rates[7,8]. With the increasing demand for data traffic by users, licenses for spectrum resources will become expensive and scarce[9]. It is unlikely that a single communication technology will be able to support these growing data demands. Therefore, future networks must support the coexistence and cooperation of different wireless

[1]School of Electronic Science and Engineering, Fujian Engineering Research Center for Solid-State Lighting, Xiamen University, Xiamen 361005, China; [2]Innovation Laboratory for Sciences and Technologies of Energy Materials of Fujian Province (IKKEM), Xiamen 361005, China; [3]Department of Photonics and Graduate Institute of Electro-Optical Engineering, College of Electrical and Computer Engineering, Yang Ming Chiao Tung University, Hsinchu 30010, Taiwan, China; [4]Semiconductor Research Center, Hon Hai Research Institute, Taipei 11492, Taiwan, China; [5]Guangdong Visible Light Communication Technology Co., LTD., Foshan 528000, China.

*Correspondence: HC Kuo, E-mail: hckuo@faculty.nctu.edu.tw; TZ Wu, E-mail: wutingzhu@xmu.edu.cn

Received: 27 October 2022; Accepted: 7 December 2022; Published online: 29 December 2022

technologies, including radio-frequency (RF), millimeter-wave, and light-wave technologies[10,11].

Light-emitting diode (LED) solid-state lighting technology offers low power consumption and cost, small size, and a long operational lifetime; moreover, it is environmentally friendly. These advantages contributed to the explosive growth of the LED-lighting market[12–18]. Notably, the visible-light band with a spectral range between 380 and 780 nm is not licensed like radio frequencies and can be used without authorization[19–23]. Hence, LED-based visible light communication (VLC) technology has attracted research attention worldwide, and VLC technology has rapidly developed in the past decade[15,24–26].

The flickering of LEDs cannot be identified by the naked eye, owing to the high frequency of the signal in the VLC system. Thus, by adding relatively inexpensive front-end components, VLC can be easily implemented in existing lighting infrastructures to achieve data communications with speeds in the Gbps range[27–31]. Furthermore, compared with the considerable co-channel interference of wireless RF communication, the propagation of visible light is not perturbed by electromagnetic waves, i.e., the electromagnetic interference phenomenon does not occur[32]. Therefore, VLC offers unique advantages in hospitals, airports, nuclear power plants, underground mines, substations, and other scenarios that are sensitive to electromagnetic interference. Accordingly, the advantages of VLC technology, such as environmental protection, stability, and confidentiality in the transmission process, make it a candidate for broad application prospects[33–35].

A unique advantage of VLC is that it can simultaneously realize illumination and displays. Owing to their high efficiency and environmental protection, white light emitting diodes (WLEDs) are considered an efficient and energy-saving solid-state light source and have received considerable attention[36–39]. Traditional WLEDs consist of blue and violet LED chips and phosphors. Despite the excellent performance of phosphor-based WLEDs, their modulation bandwidth is significantly limited by the color-conversion materials[40]. To accurately transmit high-speed data, the switching time between turning the LED on and off should be as short as possible. Thus, the device should have a short fluorescence lifetime. Therefore, the exploration of luminescent materials that can be mass-produced with high efficiency and response speed is of great significance for next-generation WLED applications.

Although LEDs have attracted considerable interest in high-speed VLC applications, many factors limit the modulation bandwidth of conventional LEDs[41,42]. Recently, research has gradually focused on the application of micro-LEDs (μLEDs) with an active area of less than 100 μm in VLC. Compared with conventional LEDs, μLEDs have a higher modulation bandwidth owing to their smaller size, higher injection-current density, and lower RC time constant, which significantly improves the transfer rate of VLC systems[43–46]. Moreover, μLEDs can be employed in displays; thus, they can be used for combined full-color display and communication applications. The compactness of μLEDs makes them easier to integrate; therefore, μLED-based VLC systems also endow wearable devices with unique advantages[47,48]. In addition, their sensitivity to light has enabled the use of μLEDs in the fabrication of high-performance receivers, which provides new possibilities for their application[49].

With the continuous advancement of 5G commercialization, future-oriented competitiveness research has begun in the field of its successor 6G[50]. The 6G white papers released by several research institutes show that 6G communication is no longer limited to the original wireless spectrum[51]. New spectrum resources can be found in the visible-light band. As one of the two major future spectrum resources, VLC can exploit the ultrahigh bandwidth in the 400–800 THz frequency range. Compared with traditional wireless frequency bands, the unlicensed spectrum used by VLC will give operators and device manufacturers more freedom, thereby establishing a technology that is suitable for 6G[52]. In the indoor environment, VLC has the inherent advantages of wide coverage, green light, and energy saving. In the outdoor environment, VLC technology can be used in underwater communication, inter-vehicular communication, and several other unique applications for realizing machine-machine interaction[53,54]. Owing to the high requirements for 6G in terms of transmission speed, VLC based on high-bandwidth μLED devices and artificial intelligence (AI) will emerge in various application fields of 6G[55]. Although μLEDs are now widely used in VLC, few studies have provided general descriptions of μLED-based VLC systems from devices to applications. An extensive review of high-speed μLED-based VLC will facilitate its comprehensive application to future 6G.

In this review, we focus on the μLED-based high-speed VLC system and its applications, as illustrated in

Fig. 1. First, the advantages and challenges of using μLEDs in VLC systems are summarized. Methods to improve the modulation bandwidth of μLEDs are comprehensively discussed, including c-polar epitaxial structure optimization, semi/nonpolar GaN epitaxial growth, microstructures, and InGaN quantum dots (QDs) as active regions. Furthermore, photoluminescent and electroluminescent WLEDs for VLC are introduced and discussed separately according to different fabrication methods. Progress in the use of μLEDs for VLC detectors is also discussed. Finally, the latest high-speed VLC applications and the application prospects of VLC in 6G are discussed.

Overview of micro light emitting diode (μLED)-based visible light communication (VLC) systems

Theory of VLC applications

The transmitter in a VLC system uses a visible-light-emitting device, such as an LED or LD, to realize data transmission[56,57]. LEDs with diffusers, energy-saving properties, and environmental protection are good light sources for providing uniform illumination. The receiver consists of a photodetector (PD) and signal-processing circuitry. After receiving the optical signal and restoring it to a current signal, the PD generates a voltage signal and completes the digital-to-analog conversion after the signal passes through the signal-processing circuit. The electrical signal is then amplified, equalized, and demodulated to extract valid data.

The channel characteristics in the VLC are distinct from those of the traditional RF system, which is mainly affected by the light source, free-space atmospheric channel, and PD at the receiving end. The modulation bandwidths of the transmitting and receiving ends jointly affect the overall performance of the VLC system. However, in most VLC systems, where the space channel is relatively stable, the devices at the transmitting end mainly affect the communication performance because of the relatively high receiving bandwidth of the PD.

Frequency response is one of the most important parameters required to address when developing LEDs for VLC-system transmitters. For a LED system, the light transfer function is expressed as follows:

$$H(\omega) = \frac{N_{\rm out}(t)}{N_{\rm in}(t)} = \frac{1}{1+{\rm i}\omega\tau}\,, \tag{1}$$

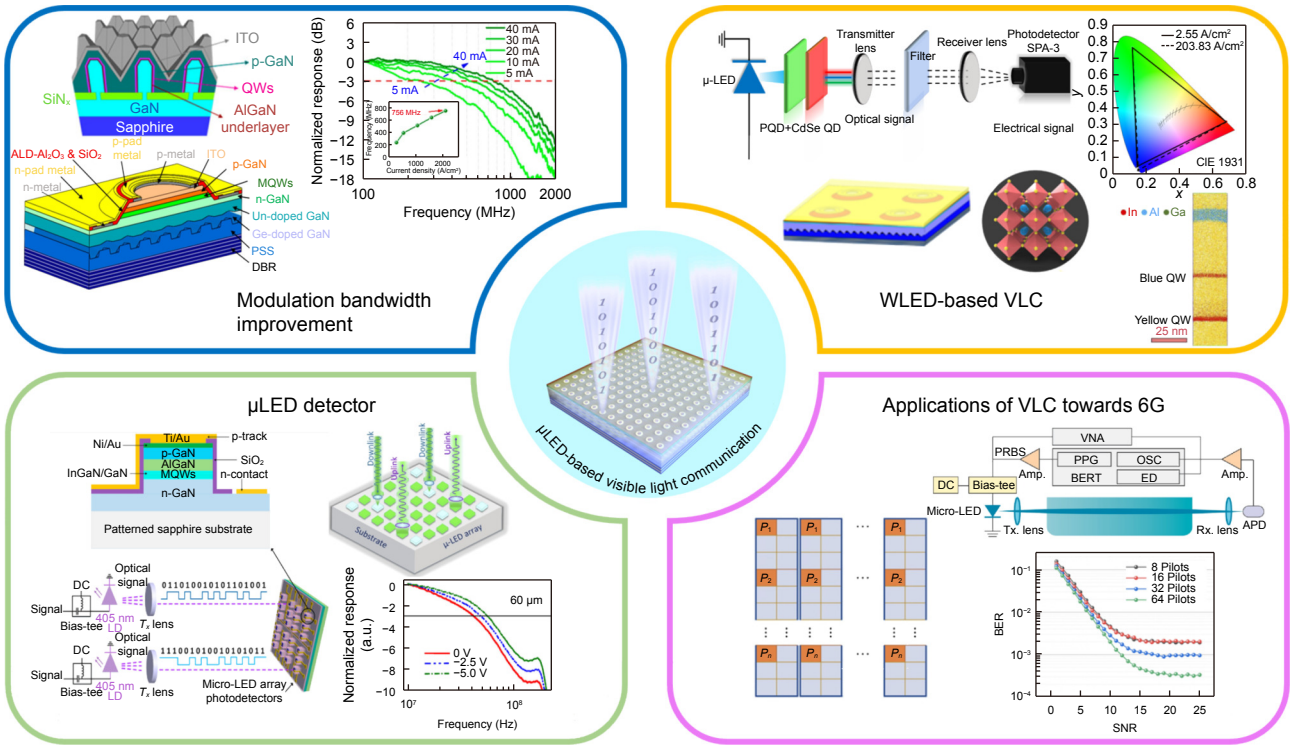

Fig. 1 | Summary of the review, which includes modulation bandwidth improvement, white light emitting diodes (WLED)-based visible light communication (VLC), micro light emitting diode (μLED) detector and applications of VLC towards 6G. Figure reproduced from: ref.[96,125,154,165], American Chemical Society; ref.[139,153], Chinese Laser Press; ref.[161,166], OSA Open Access Publishing Agreement; ref.[175,184], Optical Society of America.

where N_{in} and N_{out} are the input and output carrier concentrations, respectively. N_{out} determines the modulated optical power. ω is the angular frequency, and τ is the total response time. The frequency at which the optical modulation power is reduced by half is defined as f_c,

$$H(2\pi f_c) = \frac{1}{2}\,, \tag{2}$$

$$f_c = \frac{\sqrt{3}}{2\pi\tau} = \frac{\sqrt{3}}{2\pi}\left(\frac{1}{\tau_r} + \frac{1}{\tau_{nr}} + \frac{1}{\tau_{RC}}\right)\,, \tag{3}$$

where τ_r and τ_{nr} refer to the radiative and nonradiative recombination lifetimes, respectively. τ_{RC} is the resistor-capacitor (RC) time constant. As observed in Eq. (3), the factors affecting the LED modulation characteristics primarily depend on the RC time and carrier radiation lifetime. The junction capacitance affects the RC time and response speed of LED devices, which can delay the signals. The spontaneous emission lifetime of carriers directly affects the time required for carriers from recombination to photons to escape from the device.

Advantages of μLEDs as VLC transmitters

Commercial large-size GaN-based LED dies have an area of a few millimeters per side. However, over such a large area, the response speed is ultimately limited by its RC time constant[58]. In addition, the carrier recombination process in GaN-based LEDs is affected by the carrier localization effect and quantum confinement stark effect (QCSE), which also leads to an increased carrier lifetime and reduced electro-optical conversion response speed[59,60].

A smaller active area results in reduced geometric capacitance, and consequently a lower RC time constant, which allows μLEDs to have higher modulation bandwidths. Furthermore, μLEDs can withstand higher injection current densities, owing to their uniform current spreading. Tian et al. studied the optoelectronic properties of μLEDs of different sizes, as depicted in Fig. 2(a)[61]. The current density–voltage (J–V) curves of the LEDs are illustrated in Fig. 2(b). The results indicated that samples of different sizes exhibited strong size-dependent behavior. The smaller μLED has a more uniform current distribution, which leads to a higher injection current density[62,63]. They also demonstrated that the current crowding of large-scale samples affects efficiency, especially at high injection densities. The external quantum efficiency (EQE) of the samples was measured. As shown in Fig. 2(c), the smaller μLEDs had lower efficiencies at low current densities, and higher at high current densities. Owing to poor current uniformity, large-sized samples cause a severe efficiency decrease at higher injected carrier concentrations, which results in strong Auger recombination at the edges and other nonradiative recombinations. A higher injection current or efficiency significantly improves the performance of LEDs as VLC emitters.

Zheng et al. investigated the impact of device size

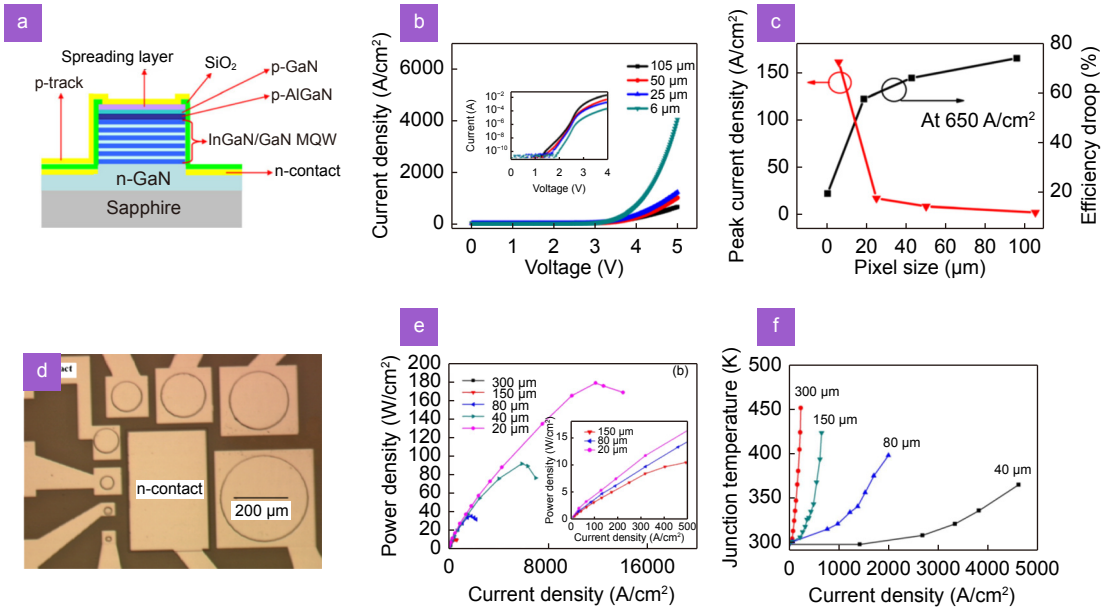

Fig. 2 | (**a**) Schematic of the samples' structure. (**b**) J–V characteristics of samples. (**c**) Current densities of peak EQE, and the efficiency drop of samples. (**d**) Optical micrograph. (**e**) Power density and (**f**) junction temperature of the samples at different current densities. Figure reproduced with permission from: (a–c) ref.[61], AIP Publishing; (d–f) ref.[64], AIP Publishing.

scaling on the light output and self-heating of InGaN LEDs[64]. Figure 2(d) illustrates the optical micrograph of samples with different sizes. The power density versus current density was measured for InGaN LEDs with diameters ranging from 20 to 300 μm (Fig. 2(e)). The study also observed that small-sized samples could withstand higher current densities. The measured junction temperature highlighted in Fig. 2(f) demonstrated that the junction temperature of the smaller samples increased more gradually with the injection current density. They specified 40 μm and 150 μm LED devices for simulation, and the current crowding effect was considered. They discovered significant overheating of the edge of the 150 μm pixel. Thus, the size-dependence effect of the junction temperature can be attributed to the more severe current crowding effect in larger pixels. This explains why smaller samples can withstand higher current densities.

In conclusion, owing to low capacitance and self-heating effect, and good current dispersion, μLEDs possess smaller RC constants and higher injection current densities than conventional wide-area LEDs, resulting in shorter carrier lifetimes and higher modulation bandwidths. Owing to the ultrasmall area, the output optical power can be increased for long-distance and high-speed communication by assembling multiple μLEDs into an array.

Challenges of μLEDs as VLC transmitters

QCSE

Although μLEDs can effectively increase bandwidth compared with traditional LEDs, they still face some challenges in VLC applications. First, commercial μLEDs are typically grown on the (0001) polar c-plane sapphire substrates. This leads to a strong QCSE, which results in reduced efficiency at high injection current densities[65]. The current GaN-based epitaxy has a hexagonal crystal structure with the highest symmetry compatibility, which results in spontaneous polarization[66]. Simultaneously, the lattice mismatch between $In_xGa_{1-x}N$ and GaN induces strain, which leads to piezoelectric polarization[67,68]. The internal spontaneous polarization and piezoelectric polarization tilt the energy-band, and reduce the radiative recombination rate of the carriers, which results in lower modulation bandwidths. In addition to the modulation properties, the QCSE also leads to a wavelength shift and efficiency decrease as the injection current density increases[69,70].

To suppress the QCSE, research has focused on optimizing the epitaxial structure of the device. For example, a thin quantum barrier (QB) can make the carrier distribution more uniform throughout the active region[71,72]. Therefore, a thin QB can enhance radiative recombination in the active region and suppress the QCSE with higher bandwidths than those of thick QB. Furthermore, the effect can also be suppressed by growing devices on semipolar or nonpolar substrates.

Carrier localization effect

At low current densities, the QCSE dominates carrier recombination and reduces the radiative recombination rate, which is the main limiting factor for the modulation bandwidth. At high injection condition, the Coulomb shielding effect reduces the polarization caused by the QCSE[73,74]. In this case, the carrier localization effect can significantly influence the carrier recombination processes.

The carrier localization effect prevents the nonradiative recombination of carriers inside the quantum well (QW), thereby increasing carrier lifetime[59,75]. Hence, for a device with a strong positioning effect, its modulation bandwidth is reduced accordingly. It has been shown that the thickness of the QW affects carrier localization. Zhu et al. fabricated μLEDs with different QW thicknesses and evaluated the extent of carrier localization[76]. For MQWs with fewer in components, the carrier localization effect was mainly caused by well-width fluctuations[77]. This suggests that the localization energy can also be evaluated using the variation of the QW band gap. Thus, thicker QW devices with lower MQW bandgap reductions have weaker carrier localization effects, and thus reduced carrier lifetimes.

Size-dependent effect

The reduced size reduces junction temperature and improves current density distribution[64,78,79]. However, as the chip size decreases to the micrometer level, the proportion of the sidewall area increases. The Schockley–Read–Hall (SRH) recombination caused by the sidewall defects in the active region affects the efficiency of the device[80]. Standard photolithographic techniques introduce severe defects on the surface during dry etching and subsequent processes, which are difficult to avoid during fabrication[61]. As the chip size decreases, the proportion of the sidewall area increases significantly,

and the effect of sidewall defects increases[81,82]. More carriers are trapped by sidewall defects during migration, which reduces the efficiency of radiative recombination[83]. In addition, the SRH recombination is weakened at high injection current densities, which leads to peak EQEs appearing at larger current densities[84].

To mitigate the performance degradation, researchers focused on eliminating the sidewall defects of μLED that cause nonradiative recombination. Passivation of sidewalls has been demonstrated as an effective method to reduce the effects of sidewall defects[83]. In addition, the sidewall defects caused by dry etching can be partially recovered by thermal annealing at high temperatures[61].

In addition, as the manufacturing technology of μLED matures, interest in μLED devices with sizes between 1 and 10 μm is increasing. Smith et al. compared the size-dependent EQE of blue and green InGaN μLEDs with sizes as low as 1 μm[85]. The results show that the EQE of blue μLED evidently decreases for smaller devices. Conversely, green wavelength devices exhibit a smaller size dependence, which is attributed to decreasing surface recombination velocities with increasing In content. Consequently, green μLED sizes smaller than 10 μm have higher EQE than blue devices.

Approaches to increasing the modulation bandwidth

μLED, as an emerging VLC emitter, has rapidly developed in recent years and has made impressive achievements. Table 1 lists the academic results of VLC systems based on μLED as a light source in recent years, which helped us gain a comprehensive understanding of the recent progress.

Currently, blue devices are the most mature among visible LEDs. Thus, blue μLEDs exhibit the highest reported modulation bandwidth among all wavelength devices. Currently, c-plane μLEDs have a lower bandwidth than nonpolar or semipolar μLEDs; however, bandwidths greater than 1 GHz can be achieved by structural optimization or growth of microstructures[86,90,95,96]. In addition, the use of QDs as active regions also helps reduce the carrier lifetime of the device[91,93]. The rest of this chapter describes the methods to increase the modulation bandwidth of the μLED device.

Optimization of C-plane epitaxial structure

InGaN/GaN MQW active regions based on c-plane growth are currently the most mature manufacturing process in the LED industry. Parameter tuning and optimization based on this structure are of great value for the future commercialization of μLED[97].

In recent years, structural optimization of c-plane μLED devices has been reported, and the improvement of the modulation bandwidth has mainly focused on enhancing the carrier recombination process. Ferreira et al. fabricated GaN-based μLEDs using Pd as the p-contact metal. Metal contacts with low contact resistances were formed by thermal annealing[98]. This helped maintain a higher current density. In addition, the face layer was etched on a sapphire substrate, which limited the matching of n-GaN to the active region, thus reducing the capacitance of the device. Rajabi et al. grew blue LEDs with ultrathin InGaN QWs (1 nm) and GaN barriers (3 nm)[70]. The ultrathin QW device was grown by metalorganic chemical vapor deposition (MOCVD) on a c-plane sapphire substrate. The epitaxial structure included a

Table 1 | Summary of research progress in the VLC system based on μLED

Year	Light source	Modulation bandwidth	Transmission rate	Ref.
2022	c-plane green μLED (525 nm)	1.31 GHz	6 Gbps	ref.[86]
2022	Semipolar blue μLED (447 nm), yellow phosphor	849 MHz	2.8 Gbps	ref.[87]
2022	c-plane blue μLED (450 nm)	880 MHz	1.1 Gbps	ref.[88]
2022	c-plane red μLED (652 nm)	271 MHz	350 Mbps	ref.[31]
2022	Nonpolar blue μLED (463 nm)	991 MHz	2 Gbps	ref.[89]
2022	c-plane blue μLED (475 nm)	1.53 GHz	5.27 Gbps	ref.[90]
2022	Green quantum dot (QD) LED (495 nm)	1.22 GHz	2.1 Gbps	ref.[91]
2021	Semipolar green μLED (550 nm)	1.1 GHz	4.3 Gbps	ref.[92]
2021	Green QD-LED (550 nm)	1.3 GHz	none	ref.[93]
2021	c-plane blue μLED (450 nm)	251 MHz	660 Mbps	ref.[94]
2021	c-plane blue μLED (467 nm)	1.3 GHz	2 Gbps	ref.[95]
2020	Semipolar green μLED (525 nm)	775 MHz	1.5 Gbps	ref.[96]

1-μm-thick GaN buffer layer, a 2.5-μm-thick Si-doped n-GaN, an MQW active region, a 30-nm-thick electron barrier layer, and a 75-nm-thick p-GaN contact layer. The sample with a thin QW/QB had a faster recombination process than that of a standard sample with a 3 nm/10 nm InGaN/GaN MQW, which was attributed to the higher EH wavefunction overlap in the thin QW. At 2.5-kA/cm^2 injection current density, the bandwidth of the thin QW/QB device was 536 MHz. Xu et al. designed and fabricated c-plane blue μLEDs with a thin InGaN layer[90]. Figure 3(a) shows a transmission electron microscopy (TEM) image of the epitaxial structure of the fabricated LED. The GaN barrier and InGaN well were 1 nm and 12 nm thick, respectively. A 3D schematic of the device is presented in Fig. 3(b), and a cross-sectional scanning electron microscopy (SEM) image of the μLED device is shown in Fig. 3(c). The 60 μm LED pixels were defined using ICP etching processes. Figure 3(d) depicts the modulation bandwidth of the μLED devices. The bandwidth eventually reaches a high value of 1.53 GHz at 6 kA/cm^2. Evidently, a 1 nm ultrathin QW structure significantly reduces the QCSE, resulting in a high recombination rate.

Dry-etching technology can cause inevitable and significant deterioration of μLED performance, and consequently cannot meet the requirements to manufacture high-performance μLEDs[29,99]. In addition, with conventional biasing methods, small changes in the forward bias will result in large fluctuations in the injection current density when the LED is operating at a high injection current density, which is difficult to maintain and control. Cai et al. demonstrated the growth of LEDs on predetermined microhole arrays created by SiO_2 masks on a high-electron-mobility transistor (HEMT) template[100]. In this study, direct modulation of the LED emission was achieved by adjusting the 50-nm HEMT gate voltage. The fabrication method is illustrated in Fig. 3(e–h). First, a SiO_2 layer was deposited on the AlGaN/GaN template. Subsequently, SiO_2 was etched into the microhole arrays. Then, metalorganic vapor-phase epitaxy (MOVPE) was used to reload the patterned HEMT template for further LED growth. The maximum modulation bandwidth

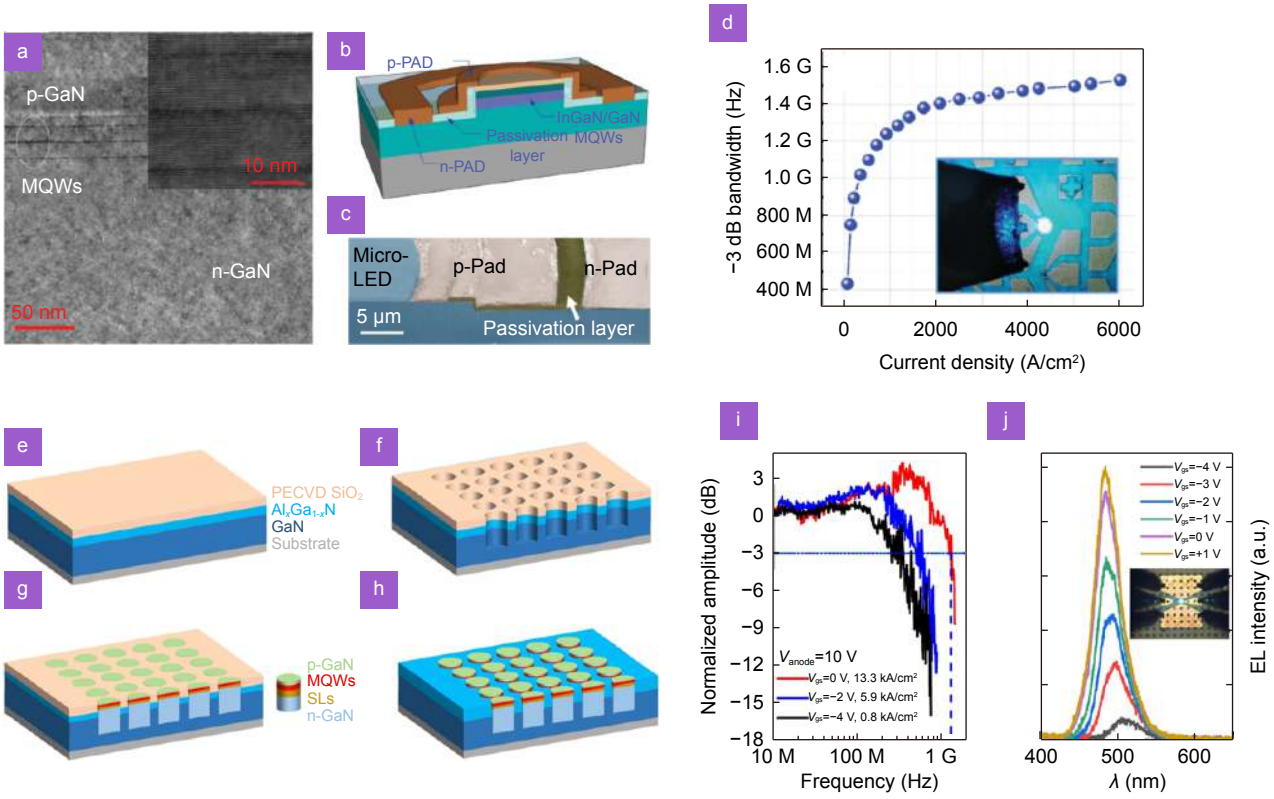

Fig. 3 | (**a**) Transmission electron microscopy (TEM) image. (**b**) Three-dimensional schematic and (**c**) scanning electron microscopy (SEM) image of a μLED. (**d**) −3 dB bandwidth for different current densities. Schematics of fabrication for the growth of μLEDs on a high-electron-mobility transistor (HEMT) template. (**e**) Deposition of SiO_2. (**f**) Fabrication of SiO_2 microhole arrays. (**g**) Growth of μLEDs. (**h**) SiO_2 mask removal. (**i**) Modulation bandwidth and (**j**) electroluminescence (EL) spectra of device. Figure reproduced with permission from: (a–d) ref.[90], IEEE; (e–j) ref.[100], under a Creative Commons Attribution (CC-BY) License.

reached 1.2 GHz (Fig. 3(i)), which was realized with a 10 V bias in relation to the HEMT and zero gate bias. Figure 3(j) shows the electroluminescence (EL) spectra of a single μLED.

Nonpolar and semipolar plane growth

C-plane LEDs are affected by a strong QCSE, which limits the modulation bandwidth and leads to a decrease in efficiency at high injection current densities[66,68]. The deleterious effects of these fields have recently sparked growing interest in nontraditional directions. One approach to overcome the QCSE is to fabricate nonpolar or semipolar structures[101]. Monavarian et al. measured the modulation bandwidths of μLEDs with different crystal orientations, as shown in Fig. 4(a)[65]. The bandwidth of the μLEDs grown on nonpolar faces is the highest, followed by those of the semipolar plane and c-plane. The difference in the bandwidth is related to the difference in the wavefunction overlap between the different crystal orientations. Corresponding to the modulation bandwidth, the wavefunction overlap is the highest in nonpolar QWs. When the growth direction of the InGaN/GaN MQW crystal planes is perpendicular to the polar plane, such as (11–20) or (1–100), the polarization field can be completely eliminated[102].

Rashidi et al. demonstrated a nonpolar m-plane blue μLED for high-speed VLC[103]. As depicted in Fig. 4(b), the device is grown on a freestanding GaN substrate formed by metal–organic chemical vapor deposition on a nonpolar (10–10) face. The normalized frequency responses of the nonpolar μLEDs at different current densities are shown in Fig. 4(c). With an injection current density of 1000 A/cm^2, the maximum –3 dB bandwidth of the LEDs reached a maximum of 1.485 GHz.

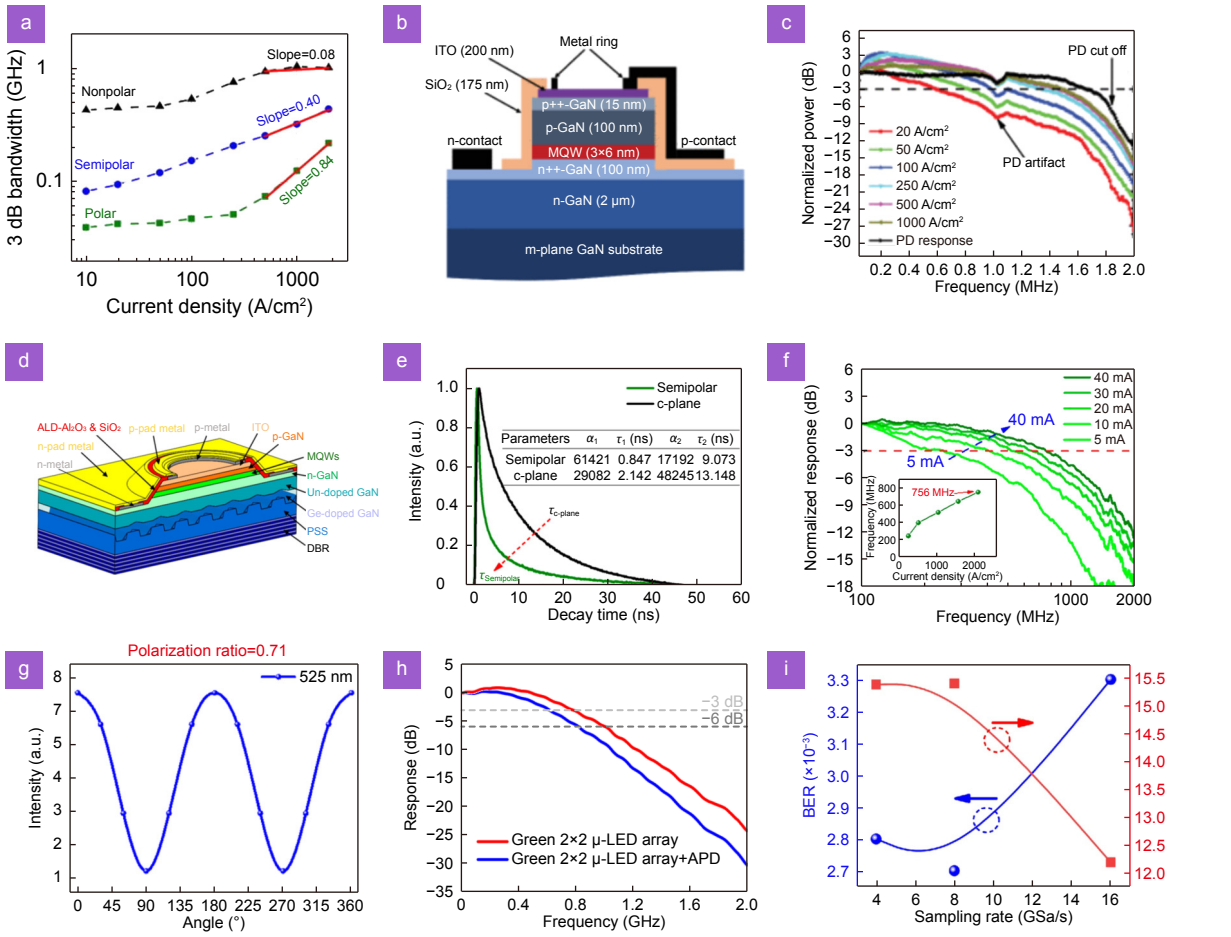

Fig. 4 | (**a**) Bandwidth for devices with different crystal orientations. (**b**) Schematic and (**c**) frequency response of the nonpolar μLED. (**d**) Schematic diagram of semipolar (20–21) green μLED structures. (**e**) Time-resolved photoluminescence (TRPL) curves of semipolar μLED and c-plane μLED. (**f**) Frequency response of the semipolar μLED. (**g**) PR and (**h**) frequency responses of μLED array. (**i**) BER and signal-to-noise ratio at 4.5 Gbit/s transmission rate with different sampling rates. Figure reproduced with permission from: (a) ref.[65], AIP Publishing; (b, c) ref.[103], IEEE; (d–f) ref.[96], American Chemical Society; (g–i) ref.[109], Optica Publishing Group.

Although devices grown on nonpolar planes can effectively eliminate polarization fields, achieving long-wavelength emissions >510 nm with such nonpolar a-plane or m-plane LEDs remains challenging. Additionally, nonpolar LEDs have a low EQE, owing to low In incorporation. The semipolar plane is also a fundamental solution to the QCSE, which makes semipolar μLEDs a strong contender for high-bandwidth devices. The chemical potential for incorporating In atoms into semipolar planes is considerably lower than that into nonpolar planes, owing to the lower repulsive interactions between the semipolar GaN surface and the In atoms. This facilitates the growth of long-wavelength InGaN/GaN devices[104]. Chen et al. realized 540-nm green μLEDs with a high −3 dB bandwidth using semipolar (20−21) GaN epitaxy[96]. Figure 4(d) demonstrates the optimized μ-LED device structure. The Al_2O_3 layer deposited by atomic-layer deposition (ALD) reduced the effect of sidewall defects. The carrier lifetime τ of the semipolar μLED measured by time-resolved photoluminescence (TRPL) is 2.65 ns, as shown in Fig. 4(e), which is much lower than that of the c-plane μLED used as a reference. The shorter lifetime of the semipolar samples is owing to the weak polarization field. This results in a larger electron-hole wavefunction overlap, which reduces τ_r[105−107]. A shorter carrier recombination corresponds to faster carrier transport; thus, green semipolar μLEDs can achieve −3 dB bandwidths up to 756 MHz, as shown in Fig. 4(f).

The fast response time and small size of semipolar μLEDs enable a high output power, high modulation bandwidth, and high efficiency when integrated into arrays[108]. Lin et al. designed a 2×2 semipolar green μLED array with a size of 50 μm[109]. Semipolar (20−21) oriented GaN layers were synthesized on a patterned sapphire substrate. All the elements in the μLED array were connected in parallel. The device was fabricated by employing nanostructured grating patterns, which improved the polarization ratio (PR)[110]. Figure 4(g) reveals that the output degree of polarization (DOP) of the semipolar μLED increased by 0.71 to favor liquid-crystal display applications. With an injected current of 23 mA, the −3 dB bandwidth of the μLED array was 800 MHz, as shown in Fig. 4(h). A transmission rate of 4.5 Gbps can be achieved using 8-QAM OFDM modulation, as shown in Fig. 4(i).

InGaN QDs in active region

GaN-based QDs have received significant research attention, owing to their strong quantum-confinement capabilities[111−114]. Unlike QWs, which only bear compressive stress from the direction parallel to the interface, the compressive stresses on QDs in three dimensions cancel each other; thus, the strain is smaller than that of QWs. In addition, QDs exhibit a stress-releasing mechanism during epitaxy[115]. Incidentally, the use of QDs instead of QWs can reduce the volume of the active region, which is beneficial for accelerating the carrier recombination process and increasing the device modulation bandwidth.

Based on the potential of GaN-based QDs devices in VLC applications, Wang et al. grew self-assembled QDs in the Volmer-Weber mode[93]. This resulted in QDs without a wetting layer (WL), owing to a sufficiently large lattice mismatch. The WL in the QD decreases the carrier localization, thereby limiting the recombination and increasing the carrier lifetime[112]. Thus, the bandwidth of the μLED device reaches 1.3 GHz at a relatively low current density of 509 A/cm^2.

QCSE suppression was also observed in QD-based long-wavelength LEDs, with a blue-shift level similar to those of nonpolar or semipolar plane devices with increasing injection current[116,117]. Wan et al. demonstrated a phosphor-free single-chip WLED using a InGaN QDs structure[118]. Figure 5(a) shows a schematic of the epitaxial structure. A HRTEM image of the MQW region is shown in Fig. 5(b), where alternately stacked light and dark layers represent GaN QBs and InGaN QWs, respectively. The modulation bandwidth of the WLED at different current densities is summarized in Fig. 5(c). The bandwidth of a traditional WLED (a few MHz) is much lower than that of the fabricated WLED. One reasonable explanation is that the QCSE of InGaN/GaN QDs is smaller than that of the InGaN/GaN QWs. The −3 dB bandwidth reached a maximum of 150 MHz. Eye diagrams for transmission rates of 50 and 127 Mbps are shown in Fig. 5(d). Wei et al. designed a green μLED with five-layer InGaN QDs[91]. Figure 5(e) shows a TEM image of the 5-layer InGaN QD structure as the active region. The heights of QDs are distributed over approximately 2−3 nm, and the horizontal distribution is denser, which helps shorten the carrier recombination lifetime. Figure 5(f) shows the extracted −3 dB bandwidth. The bandwidth of QD green μLEDs with 50 and 75 μm active region diameters can reach 1.22 and 1.14 GHz, respectively. As shown in Fig. 5(g), the 75 μm sample can achieve a maximum transmission rate of 2.0 Gbps.

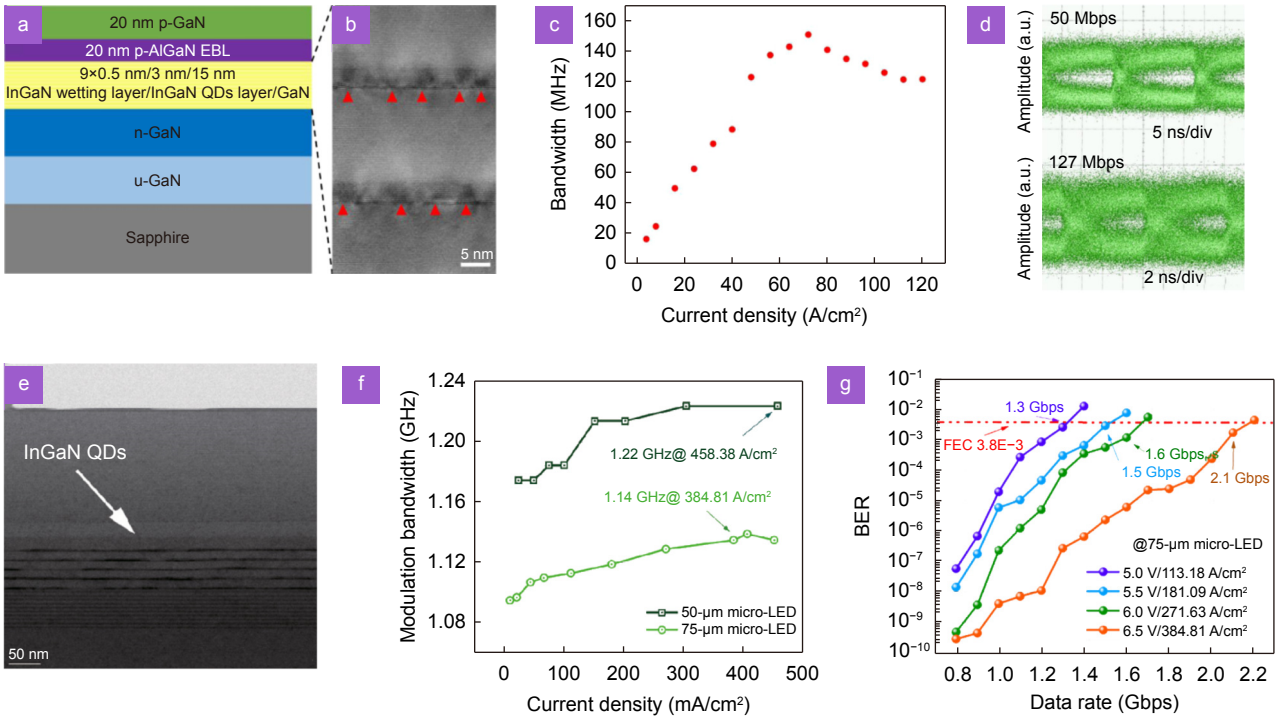

Fig. 5 | (**a**) Schematic. (**b**) HRTEM image of the QWs. (**c**) Bandwidth of single chip WLED vs. injection current density. (**d**) Eye diagram at transmission rate of 50 and 127 Mbps. (**e**) TEM images of InGaN QDs. (**f**) –3 dB bandwidth and (**g**) BER at different current densities. Figure reproduced with permission from: (a–d) ref.[118], Optica Publishing Group; (e–g) ref.[91], ACS Publishing.

Microstructure

Exploiting nanostructures in the active region to excite resonant interaction between QWs and QDs in QD-LEDs is another approach to fabricate high-modulation bandwidth devices. Nonradiative resonance energy transfer (NRET) between QWs and QDs has been demonstrated to use exciton-exciton coupling to accelerate the recombination rate[119–121]. Wan et al. fabricated quantum-well-QD-SP coupled LEDs in nanopore LED (H-LED) structures filled with QD and silver nanoparticles, which had a shorter carrier lifetime compared to H-LED and QD-only filled samples (QD-LEDs)[122]. In QD-LEDs, excitons close to the nanohole sidewall can undergo NRET. This process can significantly increase the decay rate of excitons in QWs and lead to shorter carrier lifetimes. Owing to the NRET, the recombination of excitons in the QWs of quantum-well-QD-SP coupled LEDs is faster than that of QD-LEDs, which further decreases the fast carrier lifetimes.

Similar to QDs, InGaN nanowires are another low-dimensional structure. Unlike planar μLEDs, nanowire μLEDs have independent nanowires within each pixel. Thus, the surface-to-volume ratio remains constant for different pixel sizes[123,124]. This enables a higher efficiency in nanowire μLEDs. Nanowire-based LEDs can also be considered in VLC applications. Nami et al. grew GaN nanowires on c-plane sapphire substrates using MOCVD[125]. InGaN/GaN QW/barriers were grown around the core-shell nanowires and 60 μm nanowire μLEDs were fabricated. SEM images of the nanowires after QW and p-GaN growth and the fully fabricated nanowire μLED device are shown in Fig. 6(a–c), respectively. The nanowires contained nonpolar m-plane sidewalls. The bandwidth of the nanowire μLED was 1.19 GHz, as shown in Fig. 6(d). The high modulation bandwidth of nanowire μLEDs is the result of electron-hole wavefunction overlap in nonpolar QWs, which increases the rate of recombination processes.

Recently, plasmonic devices have received extensive attention in the field of VLC for surface plasmons, which can create energy transition channels for electron-hole pairs in devices via QW-SP coupling[122]. Possible resonant coupling conditions between QWs and bulk silver have been reported[126]; therefore, the plasmonic coupling is extensively used in GaN-based LEDs[127,128]. Ferrari et al. fabricated a nanostructured plasmonic light-emitting diode (PLED)[129]. Nanoholes were patterned into the MQW region through the p-GaN layer and then coated with a thin Ag film. This scheme exploits the nanostructural properties of silver films to couple SPP to the far field.

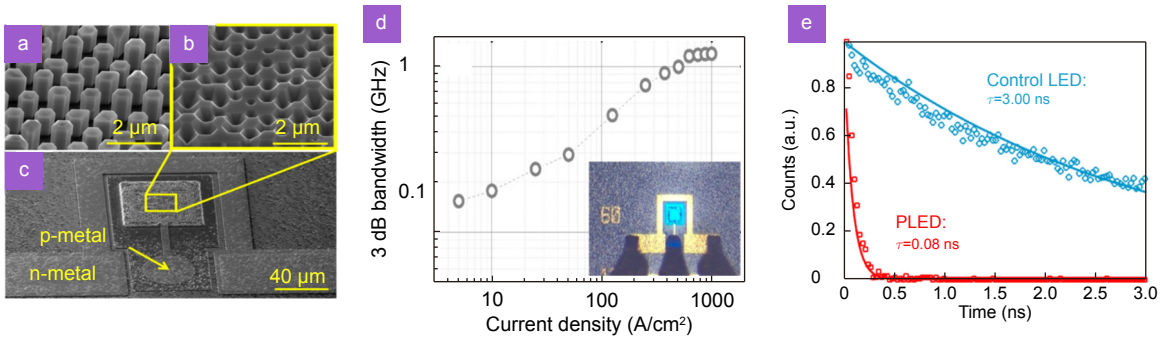

Fig. 6 | SEM images of the nanowires after (**a**) QW and (**b**) p-GaN growth and (**c**) the fully fabricated nanowire μLED device. (**d**) −3 dB bandwidth of device. (**e**) TRPL of PLED and control LED. Figure reproduced with permission from: (a–d) ref.[125], American Chemical Society; (e) ref.[129], American Chemical Society.

The decay curves of the PLED versus the control LED are shown in Fig. 6(e). The lifetimes of PLED and control LED are 0.08 ns and 3 ns, respectively, which is equivalent to a shortening by a factor of several dozen. This paves the way for the fabrication of high-speed ion-enhanced μLEDs used for VLC.

μLED-based WLED VLC system

VLC technology enables LED-based lighting infrastructure to offer both lighting and data communication. According to statistics, lighting electricity accounts for approximately 20% of the global electricity consumption, which urgently requires the development of efficient and environmentally friendly lighting sources. Therefore, compared with monochromatic blue or green LEDs, WLEDs that can provide lighting functions while offering a high luminous efficiency, long service life, and environmental protection characteristics have greater application prospects in VLC. In recent years, VLC systems utilizing WLEDs have been demonstrated[130–132].

PL WLEDs

WLEDs based on μLEDs are attractive, owing to the characteristics of a high modulation speed, high efficiency, and long lifetime. The ideal white μLED is a monolithic integration of three separate μLED chips containing red, green, and blue (RGB) emissions. Research on high-efficiency blue μLEDs is relatively mature. However, the "green gap" limits the performance of the green μLED[133]. Green μLEDs have a high proportion of indium, which requires a relatively low temperature when fabricating, which leads to strong QCSEs and a reduced radiative recombination efficiency. In addition, red μLEDs are mainly fabricated using the AlGaInP material system, which leads to long carrier diffusion length and enhanced non radiation recombination[134,135]. Therefore, the efficiency degradation of red μLEDs is more severe with the size of devices decreasing to a few microns. Another problem with implementing RGB μLEDs is that the working voltage between different pixels is different, which complicates driver circuit design. For photoluminescent WLEDs, trichromatic components are typically derived from emissive materials pumped by blue or UV chips.

WLEDs based on phosphor film for VLC

Phosphor-based WLEDs based on blue LEDs exciting yellow phosphor are among the most common lighting devices. However, the modulation bandwidth of WLEDs is significantly limited by the long response time of LEDs and fluorescent materials. This leads to difficulties in realizing high-speed VLC with the electro-optic (EO) bandwidth of conventional WLEDs of only a few MHz. Therefore, previous studies have proposed several methods to increase speed, including the addition of equalization circuits or higher-order modulation methods. Minh et al. increased the bandwidth of a WLED to 50 MHz using an analog equalizer and achieved a transmission rate of 100 Mbps[136]. Hsu et al. proposed the use of adaptive Volterra filtering for phosphor-based WLED VLC systems, and a transmission rate of 700.68 Mbit/s was achieved[137]. Hsu et al. demonstrated a 3 × 3 multiple-input multiple-output (MIMO) WLED VLC system with a data rate of 1 Gbps using a pre-equalizer circuit and OFDM modulation[138].

To address the low modulation bandwidth of WLEDs fabricated based on phosphor films, blue μLEDs can be integrated with color-conversion materials. Chun et al. achieved high-speed transmission of 1.68 Gbps using a blue μLED combined with phosphor films[139]. Huang et

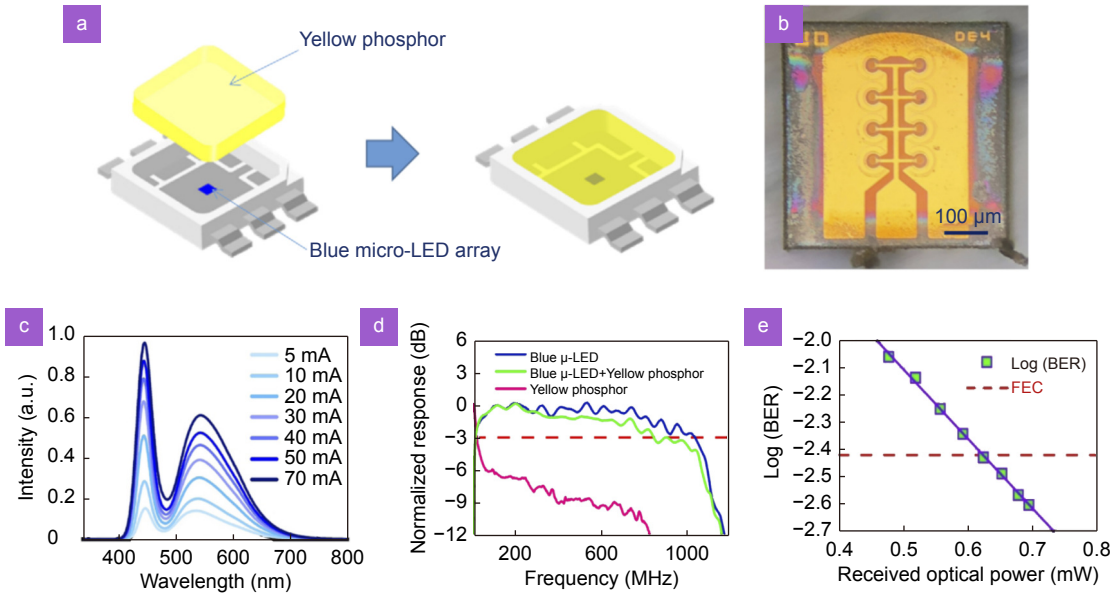

Fig. 7 | (**a**) Schematic diagram of WLED device based on semipolar μLED array. (**b**) Photographs of the μLED array without current. (**c**) Spectrum of the WLED. (**d**) Measured normalized frequency response of μLED array. (**e**) BER curve of the white-light VLC system. Figure reproduced with permission from: (a–e) ref.[87], under the Optica Open Access Publishing Agreement.

al. proposed a white-light system based on blue μLED arrays with phosphor color conversion to achieve a 127.3 MHz EO bandwidth[140]. Semipolar μLEDs also provide unique advantages in WLED systems, owing to their excellent performance. Zhang et al. utilized semipolar (20–21) blue μLEDs to pump yellow phosphors to realize a high-speed VLC system[87]. A phosphor film was coated onto the surface mounted devices (SMD) package to generate white light, as shown in Fig. 7(a). Figure 7(b) shows a photograph of the fabricated WLED device. The optoelectronic and communication properties of these devices were also evaluated. The spectrum of the blue μLED array with yellow phosphor is displayed in Fig. 7(c), with peak wavelengths of 447 and 545 nm. The normalized frequency response of the μLED array was measured, as shown in Fig. 7(d). The bandwidth of the semipolar blue μLED, yellow component and the overall white-light VLC system are 1042.5, 24, and 849 MHz, respectively. Figure 7(e) shows the BERs curves of the white-light VLC system. A data rate of 2.805 Gbps can be achieved using OFDM modulation; thus, this phosphor-based white μLED device can be applied to high-speed VLC.

WLEDs based on QDs color conversion for VLC

Despite the excellent performance of phosphor-based WLEDs, their modulation bandwidth is significantly limited by the color-conversion materials. The radiative relaxation of phosphors is related to the trap energy state with a certain depth, which causes the afterglow lasting a few microseconds[37,141–143]. Therefore, the development of color-conversion materials with a fast response speed is crucial for VLC applications. QDs are nanoscale semiconductor crystals that can modulate the emission wavelength by changing sizes[144–146]. Compared to traditional fluorophores, QDs have a wide range of absorption spectra, including blue and UV bands[147,148]. More importantly, for VLC applications, QDs typically have short fluorescence lifetimes in the order of nanoseconds. Therefore, QD-based color-conversion layers can achieve high modulation bandwidths and high data rates. Ruan et al. demonstrated that $AgInS_2$/ZnS core/shell QDs are good color-conversion materials for WLEDs and can conduct VLC[149]. Xiao et al. increased the modulation bandwidth of QD-WLED by 67.75% using CdSe/ZnS QDs[130]. Cao et al. used GHz high-bandwidth blue LED devices combined with CdSe/ZnS QDs to achieve white light emission with an overall modulation bandwidth of 637.6 MHz for visible light communication[150].

Halide perovskite quantum dots (PQDs) exhibited narrow emission and short fluorescence lifetimes and have garnered broadening research interest for VLC[151]. Shi et al. combined blue GaN-based μLEDs with $CsPbBr_{1.8}I_{1.2}$ yellow PQDs for color conversion to fabricate a white-light VLC system, as illustrated in Fig. 8(a)[152]. Modulation bandwidths of 73 MHz and 85 MHz were achieved for PQDs and overall VLC system, respectively.

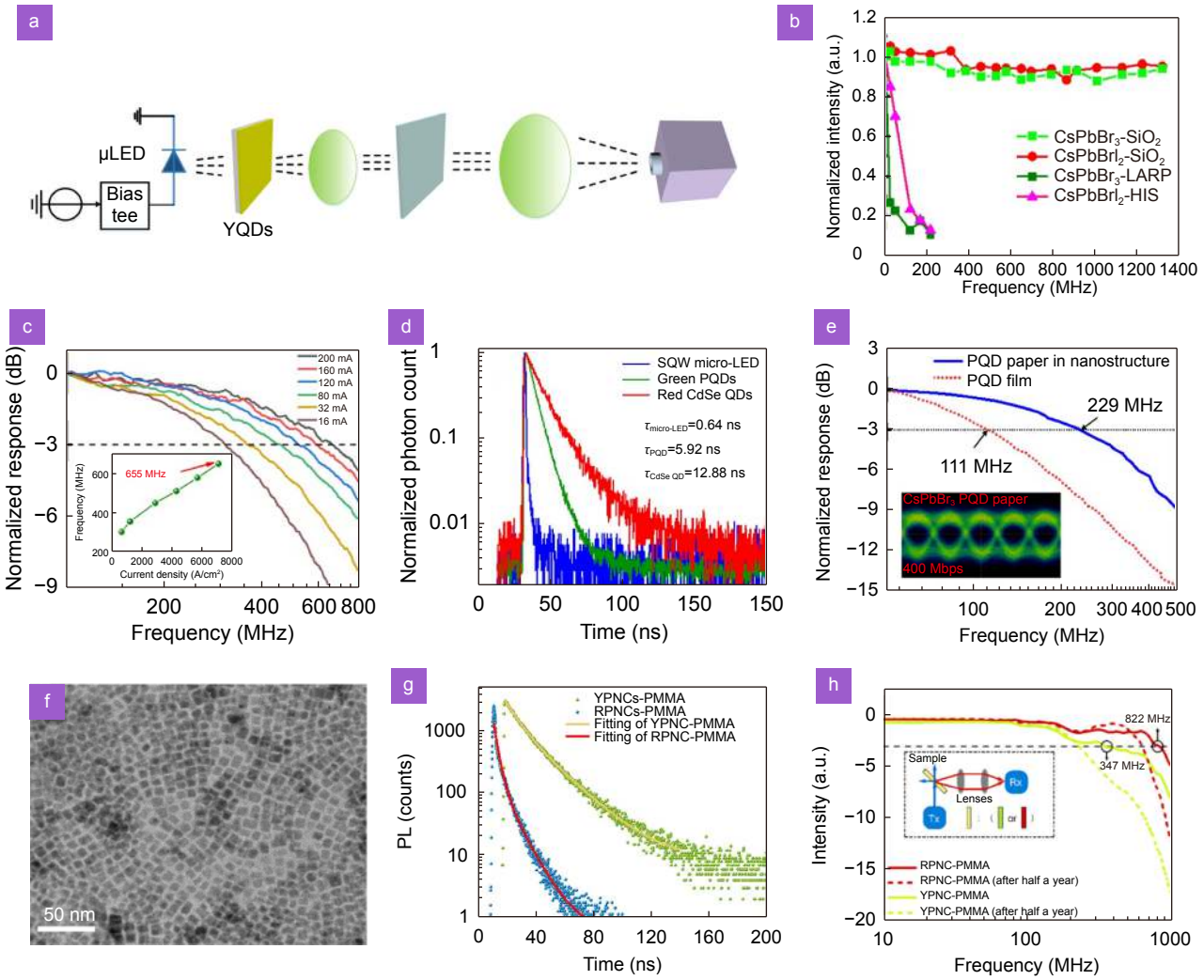

Fig. 8 | (**a**) White-light VLC system consisting of perovskite quantum dot (PQD) and blue μLED. (**b**) The longevity of the PL properties of the PNCs. (**c**) Frequency response of the PNC-μLED. (**d**) TRPL measurement for semipolar μLED, PQD and CdSe QD papers. (**e**) Frequency response of PQD paper and PQD film. (**f**) TEM images of RQDs. (**g**) TRPL measurement for YQDs and RQDs. (**h**) Frequency response of red and yellow PNC-PMMA. Figure reproduced with permission from: (a) ref.[152], American Chemical Society; (b, c) ref.[139], American Chemical Society; (d, e) ref.[153], Optica Publishing Group; (f–h) ref.[154], American Chemical Society.

Wu et al. proposed a PNC-μLED device based on a semipolar (20 –21) blue μLED array, mixing green $CsPbBr_3$ and red $CsPbBrI_2$ PNCs powders as the color conversion layer[139]. The PNCs were encapsulated in a SiO_2 shell using high-temperature sintering, which significantly improved the stability. Figure 8(b) illustrates the PL intensity of PNCs after blue radiation aging. The SiO_2-embedded samples exhibited remarkable stability and no degradation under blue irradiation. The bandwidth of PNCs is typically in the order of tens of MHz, and a filter was used to remove the red and green light generated by PNCs in the experiment. The blue light passing through the filter was coupled to a photodetector, and the highest bandwidth of the PNC-μLED was measured as 655 MHz at a current of 200 mA (Fig. 8(c)).

Currently, the in-depth study of PQDs is committed to fabricating color-conversion layers with higher modulation speeds, which will further increase the transmission rate. Singh et al. proposed a flexible white-light VLC system consisting of nanostructured green $CsPbBr_3$ PQD paper, red CdSe QD paper, and semipolar blue μLEDs[153]. $CsPbBr_3$ PQD paper was prepared by mixing a QD solution with a cellulose nanocrystal suspension. The PQD paper fabricated using this method has a nanostructure that provides a strong quantum confinement effect to increase the recombination rate. The TRPL measurements of PQD and CdSe QD are shown in Fig. 8(d), and the calculated average lifetimes are calculated as 5.92 and 12.88 ns, respectively. The shorter carrier lifetime of the PQD paper is attributable to the quantum confinement

effect. The PQD paper exhibits a higher bandwidth of 229 MHz compared to the 111 MHz of the PQD film embedded in the polymer fabrication, as shown in Fig. 8(e), which is suitable for achieving a high-speed VLC. Wang et al. proposed a white-light VLC system using red/yellow-emitting $CsPb(Br/I)_3$ and $CsPbI_3$ PNC-PMMA films combined with blue μLEDs[154]. Figure 8(f) shows the TEM images of RQDs with an average size of 5.73 ± 0.95 nm. The carrier lifetimes of yellow PNC-PMMA and red PNC-PMMA are 11.2 and 3.5 ns, respectively, as shown in Fig. 8(g). Such short lifetimes indicate a higher modulation bandwidth. This was primarily attributed to the small average size of the red QDs, which led to significantly accelerated carrier relaxation rates. The normalized frequency response of the PNC film was further tested (Fig. 8(h)). The –3 dB bandwidths of red and yellow PNC-PMMA were 822 and 347 MHz, respectively, which exhibited good potential for indoor high-speed white-light communication systems.

Notably, PQDs contain toxic elements, such as Pb and Cd, which cause pollution and limit the wide application of QDs. The fabrication of QDs without toxic elements has become a subject of intense interest recently. Soheyli et al. reported a novel aqueous-phase approach for the preparation of multicomponent In-based QDs[155]. The absorption and photoluminescence emission spectra of the as-prepared QDs were optimized by altering their composition to obtain Zn-Ag-In -S/ZnS and Cu-Ag-In-S/ZnS QDs. In addition to displays, such QDs are equally promising for VLC applications.

Electroluminescent WLEDs

Although WLEDs based on color-conversion layers have made significant progress and possess a relatively high luminous efficiency, we emphasize that such a WLED involves energy loss during the down-conversion process. The current efficiency (defined as the ratio of luminance to current) of color-conversion-based WLEDs is lower than that of electroluminescent multicolor QW WLEDs. Therefore, electroluminescent WLEDs without color-conversion layers or phosphors are attractive because they can overcome the drawbacks of phosphor-converted WLEDs, such as Stokes energy conversion loss, and they have good stability[156,157].

Blue and yellow QWs are typically grown on GaN substrates to produce monolithic WLED devices. During fabrication, the device structure is optimized to realize WLED devices more suitable for VLC. Semipolar GaN materials have high polarization ratios, a large wavefunction overlap, and short carrier lifetimes, which make monolithic white semipolar GaN μLEDs more attractive. Khoury et al. grew high-efficiency monolithic white semipolar (20–21) LEDs on 4-inch sapphire templates[158]. An overall PR of 0.3 was achieved based on the blue and yellow QWs. The μLEDs in their work achieved high modulation bandwidths of up to 660 MHz. They also reported that the PR increased in devices with longer wavelengths at higher compositions, which suggests that monolithic white semipolar LEDs have potential applications as LCD backlights[159,160].

In another study, Li et al. fabricated white semipolar (20–21) μLEDs by adopting a top blue QW and bottom yellow QW directly grown on a (20–21) semipolar bulk GaN substrate[161]. The QWs comprised a 3 nm $In_{0.28}Ga_{0.72}N$ yellow QW and a 3 nm $In_{0.13}Ga_{0.87}N$ blue QW. Figure 9(a) shows the reconstruction side view of the blue and yellow QW and EBL layers. Blue and yellow QWs with different In compositions are clearly observed. Figure 9(b) illustrates the distribution analysis of the In components in blue and yellow QWs. Subsequently, the communication performance of the μLED device was tested. Figure 9(c) indicates the modulation bandwidth for semipolar white μLEDs of all sizes. Devices with sizes of 20 and 40 μm achieved high modulation bandwidths of up to 410 MHz. Haggar et al. fabricated green, yellow, and amber semipolar LEDs on semipolar (11–22) GaN on m-plane sapphire substrates[162]. InGaN SQWs with different In components were used to achieve long-wavelength emissions of different colors. Because all the samples were fabricated using the same material system, a white-light monolithic LED chip can be integrated. The performance of the samples as VLC transmitters was measured. Figure 9(d) shows the received power spectrum of the adaptively loaded OFDM waveform, with maximum data rates of 4.42 Gbps, 3.72 Gbps, and 336 Mbps for the green, yellow, and amber devices, respectively. Figure 9(e) shows the corresponding constellation diagram.

VLC based on μLED detector

As discussed in the previous section, μLEDs with unique properties have been widely used as the transmitter in VLC. However, relatively few studies have used μLEDs as light receivers. Owing to their sensitivity to light, LEDs can potentially be used as PDs. Most commercial PDs are based on Si or GaAs, and the receiving spectrum covers a

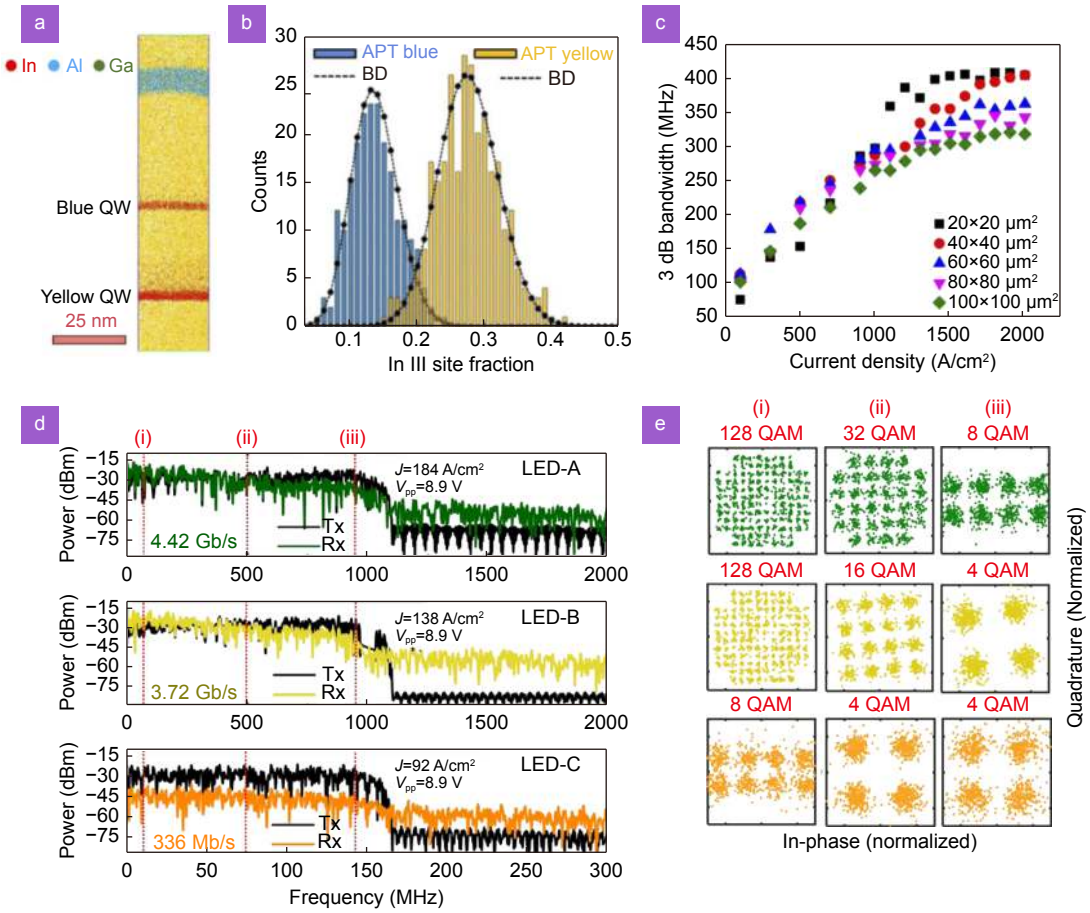

Fig. 9 | (**a**) Composition of WLED active region. (**b**) The distribution analysis of In components in QWs. (**c**) Modulation bandwidths of different sizes μLEDs. (**d**) Power spectra of OFDM-modulated waveforms measured at data rates of 4.42 Gbps, 3.72 Gbps, and 336 Mbps. (**e**) Constellations under corresponding order QAM modulation. Figure reproduced with permission from: (a–c) ref.[161], under the OSA Open Access Publishing Agreement; (d, e) ref.[162], under a Creative Commons Attribution (CC-BY) License.

wide range, which causes significant optical noise. In addition to the advantages of low dark current and high sensitivity, GaN-based LEDs offer wavelength selectivity when used as PDs and can only receive light waves lower than their own wavelengths; that is, they have natural filtering properties[43,163,164]. This topic has attracted significant academic interest. There is no need to change the MQW structure or the material of the μLEDs used as PDs. Based on the photoelectric effect, photogenerated electron–hole pairs can realize optoelectronic (OE) conversion when the MQW is excited by the input optical signal. Although the responsivities of μLED-based detectors are generally lower than those of Si or GaAs receivers, they are comparable. Owing to the wavelength selectivity of LED detectors, a higher sensitivity can be achieved for a certain band than current commercial Si or GaAs receivers[165]. In addition to the advantages of LED-based PDs, μLED-based PDs show great potential for realizing high-speed MIMO VLC for light detection. Owing to the small size and easy integration of μLEDs, μLEDs array-based PDs can enable multi-user communication and increased data rates, compared with individual μPDs. Thus, μLED displays can be used as both transmitters and detectors to achieve duplex high-speed VLC.

As part of the μLED array for VLC detectors, Liu et al. proposed a blue μLED array for use as a PD in VLC[165]. That study realized a μLED PD-based 2 × 2 MIMO VLC (Fig. 10(a)). Two LDs were used as transmitters, and a μLED array was used as the detector. Figure 10(b) illustrates the I–V characteristics of the μLED PD measured in the dark and under illumination. As observed in the figure, the current of the μLED PD gradually increases with the increase in the received power, owing to the photogenerated carriers. Additionally, for μLED-based PDs, at zero bias, high photosensitivity was observed owing to the low dark current. Figure 10(c) shows the measured responsivity of the μLED PD for different

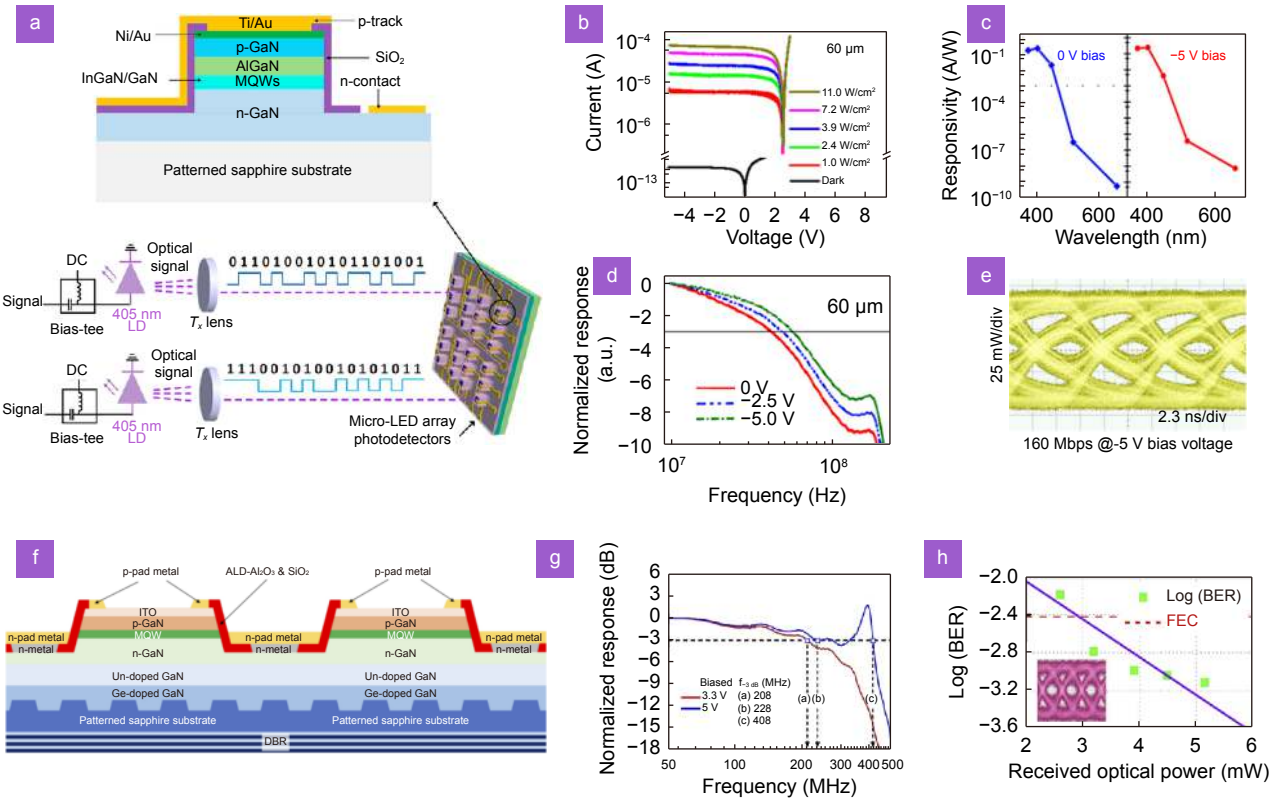

Fig. 10 | (**a**) Cross-section of the μLED and schematic setup for VLC system using the μLED based photodetectors. (**b**) Current–voltage (I–V) curves of the μLED-based PD with diameters of 60 μm under darkness and illumination. (**c**) Responsivities of the μLED-based PD measured for various laser wavelengths. (**d**) Frequency response for μLED-based PD. (**e**) Eye diagrams at a transmission rate of 160 Mbps. (**f**) Cross-section of semipolar green μLEDs. (**g**) Frequency responses of μLED PD. (**h**) BERs with μLEDs as PD at a transmission rate of 540 Mbps. Figure reproduced with permission from: (a–e) ref.[165], American Chemical Society; (f–h) ref.[166], under the OSA Open Access Publishing Agreement.

wavelength bands. The figure reveals that the μLED PD does not respond to wavelength bands above 450 nm, reflecting outstanding wavelength selectivity. The frequency response characteristics of μLED PDs under 405-nm LD illumination are illustrated in Fig. 10(d). Bandwidths up to 41.2 MHz can still be achieved at 0-V bias. Figure 10(e) shows an eye diagram captured by the μLED PD at a transmission rate of 160 Mbps and a bias of −5 V. The obtained results demonstrate the ability of μLED PDs to detect fast optical signals for high-speed communications.

In the previous discussion, we stated that semipolar μLEDs had a high application potential as VLC transmitters, owing to their higher response speed. However, semipolar μLEDs can also achieve high-speed signal detection, owing to their shortened carrier lifetime. Chang et al. investigated the performance of green semipolar (20–21) μLEDs as VLC photoreceivers[166]. The cross-section of the semipolar μLED array used as a PD with a diameter of 30 μm is illustrated in Fig. 10(f). Devices grown in the semipolar direction can provide higher modulation responses, owing to the larger overlap of electron-hole wave functions and shortened carrier lifetime. A VLC system was built with the semipolar μLED as the receiver. The OE responses of the semipolar μLED PD were measured under different biases, as shown in Fig. 10(g). At a bias of 5 V, the measured 3 dB OE bandwidths are 228 MHz, which are considerably larger than those of the LED PDs and other μLED PDs. Figure 10(h) shows the experimental BER curves obtained using the μLED PD array at a data rate of 540 Mbps. This indicates that semipolar μLEDs have a high application value as PDs in high-speed VLC systems.

Novel applications of VLC towards 6G

The development of next-generation cellular networks has aimed at faster and more reliable solutions with expansive and more complex feature sets. Networks for 6G will have higher transmission speed requirements[167,168]. Studies on epitaxial design, crystal orientation, and microstructure have enabled the fabrication of μLEDs with high-speed modulation characteristics that have

demonstrated Gbps-level data throughput. This will promote the development of μLED-based VLC systems as a key wireless technology for 6G. In addition, the use of high-frequency waves raises user concerns about the potential hazards of radio frequencies to humans in these frequency bands. From this perspective, the VLC system will provide users with the option of using an RF-free connection[169]. Adding this optical-transport interface gives device manufacturers a competitive advantage. Therefore, optical wireless communications must create a viable concept that complements RF communications as part of 6G.

Underwater VLC technology

Global extensive access is an important aspect in the development of 6G. However, underwater communication, such as in the oceans, performance has always been unsatisfactory. Underwater communication technology is important for realizing the integration of a 6G network. The realization of functions, such as wireless fusion networking and noncontact interaction, between different devices in the oceans requires underwater communication support.

Acoustic waves are the most used method of underwater communication; however, they have a low carrier frequency, which leads to a limited bandwidth[170]. Although RF waves have a higher transmission bandwidth than sound waves, owing to the skin effect, the transmission distance is directly limited, making it difficult to implement the main task of 6G underwater communication[171,172]. Wavelengths between 450 and 550 nm have considerably less attenuation than other light bands, which indicates that blue–green light is of great significance in underwater communication and lays the foundation for underwater visible-light communication (UVLC). Compared with other wireless communication methods, UVLC has the advantages of high transmission rate, strong anti-interference ability, and high security[173]. μLEDs have exhibited great potential for medium/short-distance high-speed underwater transmission through a high modulation bandwidth[174].

Recently, Wei et al. fabricated a QD blue μLED with a size of 75 μm for UVLC[175]. The growth-interruption method was employed to fabricate QD active region. Figure 11(a) and 11(b) illustrate a schematic and a photograph of the experimental setup of the μLED-based UVLC system, respectively, over a 3 m communication distance. At a current density of 582.54 A/cm^2, the modulation bandwidth of the UVLC system increased to 1.03 GHz (Fig. 11(c)). Thus, a transmission rate of 2 Gbps could be achieved with a BER of 2.03×10^{-3}. Kim et al. proposed a 32 × 32 high-power MQW flip-chip blue μLED array (μLED-on-HEMT) integrated into AlGaN/GaN-based HFETs for UVLC[176]. The uniform optoelectronic properties were obtained for each pixel of the integrated μLED-on-HEMT array. The light output power (LOP) and current of the μLED-on-HEMT device were measured as functions of V_{DD} (Fig. 11(d)). The LOP was 3.7 mW, and V_{DD} was 10 V. Each pixel of the integrated array of μLEDs exhibited a high LOP of modulation at 450 nm, which demonstrated the potential for use in UVLC. Lin et al. also demonstrated that, in addition to serving as transmitters, μLEDs could realize optical detection and underwater charging in duplex UVLC[94]. At 0 V bias, the maximum transmission rate of the μLED PD-based UVLC system was 52.5 Mbps. Under a high received optical power, the device could efficiently collect photogenerated carriers. Through circuit design, the μLED can simultaneously collect DC energy that is irrelevant to the transmission information for charging, while realizing high-speed AC signal detection, which is sufficient to drive a 660 nm LD.

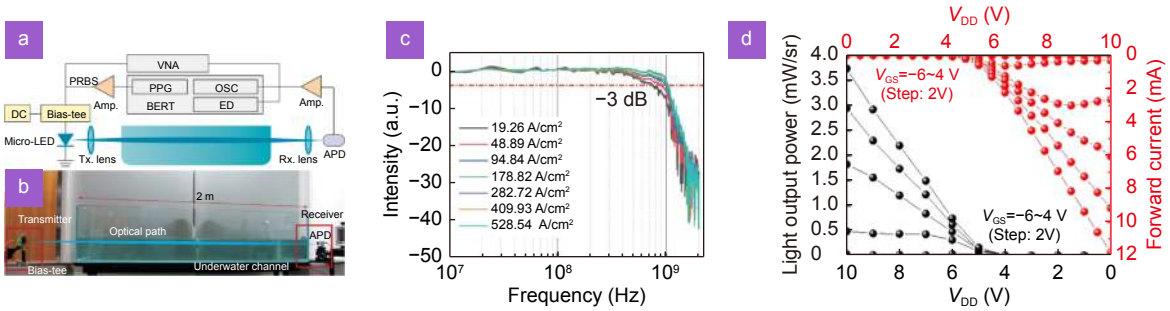

Fig. 11 | (**a**) Schematic of setup and (**b**) photograph and (**c**) frequency responses of the μLED-based UOWC system. (**d**) Light output power (LOP) and forward current characteristics of the μLED-on-HEMT arrays. Figure reproduced with permission from: (a–c) ref.[175], under a Creative Commons Attribution license; (d) ref.[176], under a Creative Commons Attribution License.

Visible light communication based on AI discipline

VLC applied to 6G must span multiple scenarios, which will lead to complex and changeable channels. Therefore, signals will be affected by nonlinear distortions during transmission. In addition to the complexity of the channel, the nonlinear response of the transmitter LED and PD may also complicate the model of the VLC system, making fitting it with traditional equalization algorithms difficult.

Recently, AI has been widely used in VLC for tasks such as higher-order modulation and demodulation, channel estimation, indoor positioning, and nonlinear equalization. Nonlinearities in high-speed VLC systems can be mitigated by employing clustering schemes and neural networks (NNs). For the application of the clustering, Lu et al. proposed the use of the K-means algorithm to cluster constellation points with a center shift under nonlinear conditions to obtain a new distribution center of constellation points under the condition of deformation[177]. Wen et al. proposed a novel sampling frequency offset mitigation scheme[178]. The algorithm was based on K-means clustering, which enabled the accurate clustering of constellation points with phase offsets. Simultaneously, with the development of GPUs and advancements in digital signal-processing technology, equalizers based on deep NNs (DNNs) are becoming popular. Chi et al. proposed a high-speed kernel-function-based DNN for nonlinear mitigation[179]. Additionally, Chen et al. proposed a hybrid frequency-domain-assisted temporal convolutional NN to compensate for the nonlinear distortions in UVLC systems[180].

To meet the requirements of ever-increasing data in the 6G era, various efforts must be made to increase the data rate to the order of 10 Gbps. From a device perspective, combining an NN-based equalizer with μLEDs with a high EO bandwidth is a feasible solution to maximize the transmitted data. In addition to DNNs, the potential of an artificial NN (ANN) program for high-speed communication owing to its approximation to arbitrary functions was demonstrated[181–183]. Wei et al. combined high-bandwidth μLED and ANN equalizers in a VLC system to achieve higher data rates. The ANN consists of five layers[184]. The training dataset was obtained from the Winner channel model dataset. The system structure is illustrated in Fig. 12(a), and a schematic of the arrangement of pilots in the OFDM symbols is shown in Fig. 12(b). The BER simulation results using blocks with pilot lengths of 8, 16, 32, and 64 were measured, as shown in Fig. 12(c). The ANN equalizer achieved relatively good results in the low signal-to-noise (SNR) range. For a specific number of pilots, the BER decreased rapidly and then settled into a higher SNR range. Based on this system, the data rate vs. BER, with two μLEDs as transmitters, was tested (Fig. 12(d) and 12(e)). The 75 μm μLED exhibited better performance and could transmit data at a rate of 8.75 Gbps.

Conclusions

As the research on μLED devices expands, the μLED-based high-speed VLC is garnering increasing interest.

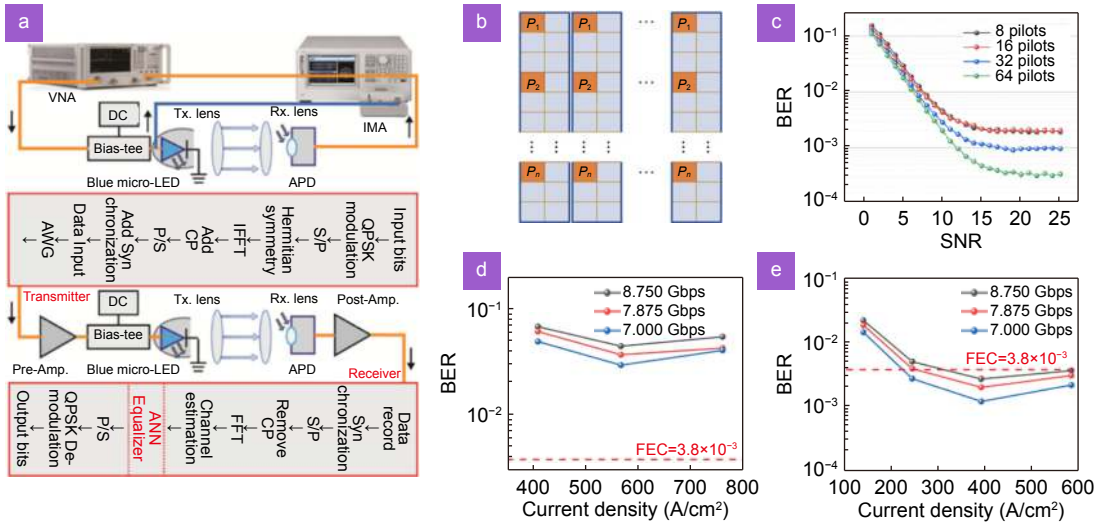

Fig. 12 | (**a**) Schematic of the VLC system based on μLED and ANN equalizers. (**b**) Schematic of the arrangement of pilots. (**c**) BER in simulation with different pilot lengths. BER performance for (**d**) 50- and (**e**) 75-μm blue μLEDs. Figure reproduced with permission from ref.[184], Optical Society of America.

This review summarizes the advantages and challenges of μLEDs in VLC systems. Methods to improve the modulation bandwidth of μLEDs were introduced. In addition to conventional c-polar epitaxial structure optimization and semi/nonpolar GaN epitaxial growth, μLEDs using microstructures or InGaN QDs as active regions can also improve the radiative recombination rate. μLEDs are considered bright solid-state lighting sources compared with different classes of WLEDs for VLC. Similarly, μLEDs can also be used as detectors in VLC systems. Finally, the prospects of VLC in 6G and the latest high-speed VLC applications were introduced. Given the high-speed transmission advantages, μLED-based VLC is expected to become an ancillary technology for 6G and cooperate with other communication technology to benefit our daily lives.

References

1. Chow CW, Kuo FM, Shi JW, Yeh CH, Wu YF et al. 100 GHz ultra-wideband (UWB) fiber-to-the-antenna (FTTA) system for in-building and in-home networks. *Opt Express* **18**, 473–478 (2010).
2. Karunatilaka D, Zafar F, Kalavally V, Parthiban R. LED based indoor visible light communications: state of the art. *IEEE Commun Surv Tutor* **17**, 1649–1678 (2015).
3. Hussain B, Li XB, Che FY, Yue CP, Wu L. Visible light communication system design and link budget analysis. *J Lightwave Technol* **33**, 5201–5209 (2015).
4. Zhang CY, Zhou W, Geng D, Bai C, Li WD et al. Laser direct writing and characterizations of flexible piezoresistive sensors with microstructures. *Opto-Electron Adv* **4**, 200061 (2021).
5. Yu KP, Tan L, Yang CX, Choo KKR, Bashir AK et al. A blockchain-based shamir's threshold cryptography scheme for data protection in industrial internet of things settings. *IEEE Internet Things J* **9**, 8154–8167 (2022).
6. Zhang JM, Harman M, Ma L, Liu Y. Machine learning testing: survey, landscapes and horizons. *IEEE Trans Softw Eng* **48**, 1–36 (2022).
7. Ahn SJ, Kim J, Kim J. The bifold triadic relationships framework: a theoretical primer for advertising research in the metaverse. *J Advert* **51**, 592–607 (2022).
8. Kwon HJ, El Azzaoui A, Park JH. MetaQ: a quantum approach for secure and qptimized metaverse environment. *Human-Centric Comput Inf Sci* **12**, 42 (2022).
9. Khan LU. Visible light communication: applications, architecture, standardization and research challenges. *Digit Commun Netw* **3**, 78–88 (2017).
10. Xu B, Sanjurjo DA, Colombi D, Törnevik C. A monte carlo analysis of actual maximum exposure from a 5G millimeter-wave base station antenna for EMF compliance assessments. *Front Public Health* **9**, 777759 (2022).
11. Li X, Tang H, Hu GB, Zhao B, Liang JR. ViPSN-Pluck: a transient-motion-powered motion detector. *IEEE Internet Things J* **9**, 3372–3382 (2022).
12. Lee JH, Islam ABMH, Kim TK, Cha YJ, Kwak JS. Impact of tin-oxide nanoparticles on improving the carrier transport in the Ag/p-GaN interface of InGaN/GaN micro-light-emitting diodes by originating inhomogeneous Schottky barrier height. *Photonics Res* **8**, 1049–1058 (2020).
13. Lee DH, Seong TY, Amano H. Stable electrical performance of AlGaInP-based red micro-light emitting diode by controlling interfacial morphologies of metal contacts. *J Alloys Compd* **872**, 159629 (2021).
14. Haigh PA, Ghassemlooy Z, Rajbhandari S, Papakonstantinou I. Visible light communications using organic light emitting diodes. *IEEE Commun Mag* **51**, 148–154 (2013).
15. Sajjad MT, Manousiadis PP, Chun H, Vithanage DA, Rajbhandari S et al. Novel fast color-converter for visible light communication using a blend of conjugated polymers. *ACS Photonics* **2**, 194–199 (2015).
16. Zhang SY, Tsonev D, Videv S, Ghosh S, Turnbull GA et al. Organic solar cells as high-speed data detectors for visible light communication. *Optica* **2**, 607–610 (2015).
17. Lu XY, Zhu SJ, Lin RZ, Sun D, Cui XG et al. Performance improvement of red InGaN micro-LEDs by transfer printing from Si substrate onto glass substrate. *IEEE Electron Device Lett* **43**, 1491–1494 (2022).
18. Fan XT, Wu TZ, Liu B, Zhang R, Kuo HC et al. Recent developments of quantum dot based micro-LED based on non-radiative energy transfer mechanism. *Opto-Electron Adv* **4**, 210022 (2021).
19. Du CH, Jiang CY, Zuo P, Huang X, Pu X et al. Piezo-phototronic effect controlled dual-channel visible light communication (PVLC) using InGaN/GaN multiquantum well nanopillars. *Small* **11**, 6071–6077 (2015).
20. Elgala H, Mesleh R, Haas H. Indoor optical wireless communication: potential and state-of-the-art. *IEEE Commun Mag* **49**, 56–62 (2011).
21. Pathak PH, Feng XT, Hu PF, Mohapatra P. Visible light communication, networking, and sensing: a survey, potential and challenges. *IEEE Commun Surv Tutor* **17**, 2047–2077 (2015).
22. Parikh H, Chokshi J, Gala N, Biradar T. Wirelessly transmitting a grayscale image using visible light. In *Proceedings of 2013 International Conference on Advances in Technology and Engineering* (*ICATE*) 1–6 (IEEE, 2013); http://doi.org/10.1109/ICAdTE.2013.6524748
23. Dede G, Kamalakis T, Varoutas D. Evaluation of optical wireless technologies in home networking: an analytical hierarchy process approach. *J Opt Commun Netw* **3**, 850–859 (2011).
24. Zhang YL, Jiang MJ, Han T, Xiao XT, Chen WL et al. Aggregation-induced emission luminogens as color converters for visible-light communication. *ACS Appl Mater Interfaces* **10**, 34418–34426 (2018).
25. Zhou ZJ, Tian PF, Liu XY, Mei SL, Zhou D et al. Hydrogen peroxide-treated carbon dot phosphor with a bathochromic-shifted, aggregation-enhanced emission for light-emitting devices and visible light communication. *Adv Sci* **5**, 1800369 (2018).
26. Khonina SN, Kazanskiy NL, Butt MA, Karpeev SV. Optical multiplexing techniques and their marriage for on-chip and optical fiber communication: a review. *Opto-Electron Adv* **5**, 210127 (2022).
27. Jovicic A, Li JY, Richardson T. Visible light communication: opportunities, challenges and the path to market. *IEEE Commun Mag* **51**, 26–32 (2013).
28. O'Brien DC. Visible light communications: challenges and

potential. In *Proceedings of the IEEE Photonic Society 24th Annual Meeting* 365–366 (IEEE, 2011); http://doi.org/10.1109/PHO.2011.6110579.

29. McKendry JJD, Massoubre D, Zhang SL, Rae BR, Green RP et al. Visible-light communications using a CMOS-controlled micro-light-emitting-diode array. *J Lightwave Technol* **30**, 61–67 (2012).
30. Zhang SL, Watson S, McKendry JJD, Massoubre D, Cogman A et al. 1.5 Gbit/s multi-channel visible light communications using CMOS-controlled GaN-based LEDs. *J Lightwave Technol* **31**, 1211–1216 (2013).
31. Huang YM, Peng CY, Miao WC, Chiang H, Lee TY et al. High-efficiency InGaN red micro-LEDs for visible light communication. *Photonics Res* **10**, 1978–1986 (2022).
32. Biagi M, Borogovac T, Little TDC. Adaptive receiver for indoor visible light communications. *J Lightwave Technol* **31**, 3676–3686 (2013).
33. Zhu SC, Yu ZG, Zhao LX, Wang JX, Li JM. Enhancement of the modulation bandwidth for GaN-based light-emitting diode by surface plasmons. *Opt Express* **23**, 13752–13760 (2015).
34. Zhao L, Cai KY, Jiang M. Multiuser precoded MIMO visible light communication systems enabling spatial dimming. *J Lightwave Technol* **38**, 5624–5634 (2020).
35. Wu HJ, Wang Q, Xiong J, Zuniga M. SmartVLC: co-designing smart lighting and communication for visible light networks. *IEEE Trans Mob Comput* **19**, 1956–1970 (2020).
36. Dursun I, Shen C, Parida MR, Pan J, Sarmah SP et al. Perovskite nanocrystals as a color converter for visible light communication. *ACS Photonics* **3**, 1150–1156 (2016).
37. Gao H, Xie YY, Geng C, Xu S, Bi WG. Efficiency enhancement of quantum-dot-converted LEDs by 0D-2D hybrid scatterers. *ACS Photonics* **7**, 3430–3439 (2020).
38. Lai SQ, Li QX, Long H, Ying LY, Zheng ZW et al. Theoretical study and optimization of the green InGaN/GaN multiple quantum wells with pre-layer. *Superlattices Microstruct* **155**, 106906 (2021).
39. Yan DD, Zhao SY, Zhang YB, Wang HX, Zang ZG. Highly efficient emission and high-CRI warm white light-emitting diodes from ligand-modified CsPbBr3 quantum dots. *Opto-Electron Adv* **5**, 200075 (2022).
40. Su CY, Wu YC, Cheng CH, Wang WC, Wang HY et al. Color-converting violet laser diode with an ultrafast BEHP-PPV + MEH-PPV polymer blend for high-speed white lighting data link. *ACS Appl Electron Mater* **2**, 3017–3027 (2020).
41. Shi JW, Sheu JK, Chen CH, Lin GR, Lai WC. High-speed GaN-based green light-emitting diodes with partially n-doped active layers and current-confined apertures. *IEEE Electron Device Lett* **29**, 158–160 (2008).
42. Ryou JH, Lee W, Limb J, Yoo D, Liu JP et al. Control of quantum-confined Stark effect in InGaN/GaN multiple quantum well active region by *p*-type layer for III-nitride-based visible light emitting diodes. *Appl Phys Lett* **92**, 101113 (2008).
43. Chen XW, Jin MY, Lin RZ, Zhou GF, Cui XG et al. Visible light communication based on computational temporal ghost imaging and micro-LED-based detector. *Opt Lasers Eng* **152**, 106956 (2022).
44. Wang YP, Chen HL, Jiang WJ, Li XY, Chen XW et al. Optical encryption for visible light communication based on temporal ghost imaging with a micro-LED. *Opt Lasers Eng* **134**, 106290 (2020).
45. Islim MS, Ferreira RX, He XY, Xie EY, Videv S et al. Towards 10 Gb/s orthogonal frequency division multiplexing-based visible light communication using a GaN violet micro-LED. *Photonics Res* **5**, A35–A43 (2017).
46. Zhu SJ, Qiu PJ, Shan XY, Lin RZ, Wang Z et al. High-speed long-distance visible light communication based on multicolor series connection micro-LEDs and wavelength division multiplexing. *Photonics Res* **10**, 1892–1899 (2022).
47. Asad M, Li Q, Sachdev M, Wong WS. Thermal and optical properties of high-density GaN micro-LED arrays on flexible substrates. *Nano Energy* **73**, 104724 (2020).
48. Lai SQ, Lu TW, Lin SH, Lin Y, Lin GC et al. Improved modulation bandwidth of blue mini-LEDs by atomic-layer deposition sidewall passivation. *IEEE Trans Electron Devices* **69**, 4936–4943 (2022).
49. Zhou GF, Lin RZ, Qian ZY, Zhou XJ, Shan XY et al. GaN-based micro-LEDs and detectors defined by current spreading layer: size-dependent characteristics and their multifunctional applications. *J Phys D Appl Phys* **54**, 335104 (2021).
50. Katz M, Ahmed I. Opportunities and challenges for visible light communications in 6G. In *Proceedings of the 2nd 6G Wireless Summit* (*6G SUMMIT*) 1–5 (IEEE, 2020); http://doi.org/10.1109/6GSUMMIT49458.2020.9083805.
51. Saud MS, Ahmed I, Kumpuniemi T, Katz M. Reconfigurable optical-radio wireless networks: meeting the most stringent requirements of future communication systems. *Trans Emerg Telecommun Technol* **30**, e3562 (2019).
52. Chi N, Haas H, Kavehrad M, Little TDC, Huang XL. Visible light communications: demand factors, benefits and opportunities [Guest Editorial]. *IEEE Wirel Commun* **22**, 5–7 (2015).
53. Li JH, Wang FM, Zhao MM, Jiang FY, Chi N. Large-coverage underwater visible light communication system based on blue LED employing equal gain combining with integrated PIN array reception. *Appl Opt* **58**, 383–388 (2019).
54. Chen M, Zou P, Zhang L, Chi N. Demonstration of a 2.34 Gbit/s real-time single silicon-substrate blue LED-based underwater VLC system. *IEEE Photonics J* **12**, 7900211 (2020).
55. Zou P, Zhao YH, Hu FC, Chi N. Enhanced performance of MIMO multi-branch hybrid neural network in single receiver MIMO visible light communication system. *Opt Express* **28**, 28017–28032 (2020).
56. Wu SE, Wang HG, Youn CH. Visible light communications for 5G wireless networking systems: from fixed to mobile communications. *IEEE Netw* **28**, 41–45 (2014).
57. Arfaoui MA, Soltani MD, Tavakkolnia I, Ghrayeb A, Assi CM et al. Measurements-based channel models for indoor lifi systems. *IEEE Trans Wirel Commun* **20**, 827–842 (2021).
58. Haemmer M, Roycroft B, Akhter M, Dinh DV, Quan Z et al. Size-dependent bandwidth of semipolar $(11\bar{2}2)$ light-emitting-diodes. *IEEE Photonics Technol Lett* **30**, 439–442 (2018).
59. Mickevičius J, Tamulaitis G, Kuokštis E, Liu K, Shur MS et al. Well-width-dependent carrier lifetime in AlGaN/AlGaN quantum wells. *Appl Phys Lett* **90**, 131907 (2007).
60. Li YL, Huang YR, Lai YH. Efficiency droop behaviors of InGaN/GaN multiple-quantum-well light-emitting diodes with varying quantum well thickness. *Appl Phys Lett* **91**, 181113 (2007).
61. Tian PF, McKendry JJD, Gong Z, Guilhabert B, Watson IM et al. Size-dependent efficiency and efficiency droop of blue InGaN micro-light emitting diodes. *Appl Phys Lett* **101**, 231110

(2012).
62. Kim H, Cho J, Lee JW, Yoon S, Kim H et al. Measurements of current spreading length and design of GaN-based light emitting diodes. *Appl Phys Lett* **90**, 063510 (2007).
63. Ryu HY, Shim JI. Effect of current spreading on the efficiency droop of InGaN light-emitting diodes. *Opt Express* **19**, 2886–2894 (2011).
64. Gong Z, Jin SR, Chen YJ, McKendry J, Massoubre D et al. Size-dependent light output, spectral shift, and self-heating of 400 nm InGaN light-emitting diodes. *J Appl Phys* **107**, 013103 (2010).
65. Monavarian M, Rashidi A, Aragon AA, Oh SH, Rishinaramangalam AK et al. Impact of crystal orientation on the modulation bandwidth of InGaN/GaN light-emitting diodes. *Appl Phys Lett* **112**, 041104 (2018).
66. Piprek J. Efficiency droop in nitride-based light-emitting diodes. *Phys Status Solidi* **207**, 2217–2225 (2010).
67. Bernardini F, Fiorentini V, Vanderbilt D. Spontaneous polarization and piezoelectric constants of III-V nitrides. *Phys Rev B* **56**, R10024–R10027 (1997).
68. Takeuchi T, Sota S, Katsuragawa M, Komori M, Takeuchi H et al. Quantum-confined stark effect due to piezoelectric fields in GaInN strained quantum wells. *Jpn J Appl Phys* **36**, L382–L385 (1997).
69. Du CH, Huang X, Jiang CY, Pu X, Zhao ZF et al. Tuning carrier lifetime in InGaN/GaN LEDs via strain compensation for high-speed visible light communication. *Sci Rep* **6**, 37132 (2016).
70. Rajabi K, Wang JX, Jin J, Xing YC, Wang L et al. Improving modulation bandwidth of c-plane GaN-based light-emitting diodes by an ultra-thin quantum wells design. *Opt Express* **26**, 24985–24991 (2018).
71. Lin GB, Kim DY, Shan QF, Cho J, Schubert EF et al. Effect of quantum barrier thickness in the multiple-quantum-well active region of gainn/gan light-emitting diodes. *IEEE Photonics J* **5**, 1600207 (2013).
72. Wang CK, Chiou YZ, Chang SJ, Chang CY, Chiang TH et al. On the effect of quantum barrier thickness in the active region of nitride-based light emitting diodes. *Solid·State Electron* **99**, 11–15 (2014).
73. Hammersley S, Watson-Parris D, Dawson P, Godfrey MJ, Badcock TJ et al. The consequences of high injected carrier densities on carrier localization and efficiency droop in InGaN/GaN quantum well structures. *J Appl Phys* **111**, 083512 (2012).
74. Bochkareva NI, Rebane YT, Shreter YG. Efficiency droop and incomplete carrier localization in InGaN/GaN quantum well light-emitting diodes. *Appl Phys Lett* **103**, 191101 (2013).
75. Malinauskas T, Miasojedovas S, Aleksiejūnas R, Juršėnas S, Jarašiūnas K et al. Direct study of nonlinear carrier recombination in InGaN quantum well structures. *Phys Status Solidi* **8**, 2381–2383 (2011).
76. Zhu SC, Lin S, Li J, Yu ZG, Cao HC et al. Influence of quantum confined Stark effect and carrier localization effect on modulation bandwidth for GaN-based LEDs. *Appl Phys Lett* **111**, 171105 (2017).
77. Li Z, Kang JJ, Wang BW, Li HJ, Weng YH et al. Two distinct carrier localization in green light-emitting diodes with InGaN/GaN multiple quantum wells. *J Appl Phys* **115**, 083112 (2014).
78. Bai J, Cai YF, Feng P, Fletcher P, Zhao XM et al. A direct epitaxial approach to achieving ultrasmall and ultrabright InGaN micro light-emitting diodes (μLEDs). *ACS Photonics* **7**, 411–415 (2020).
79. Chung KC, Lee JJ, Huang JR, Lai YJ, Chen KH et al. A dynamic compensated and 95% high-efficiency supply buffer in RGB virtual pixel microLED display for reducing ghosting by 73% and achieving four times screen resolution. *IEEE Trans Power Electron* **36**, 8291–8299 (2021).
80. Bai J, Cai YF, Feng P, Fletcher P, Zhu CQ et al. Ultrasmall, ultracompact and ultrahigh efficient InGaN micro light emitting diodes (μLEDs) with narrow spectral line width. *ACS Nano* **14**, 6906–6911 (2020).
81. Yang W, Zhang SL, McKendry JJD, Herrnsdorf J, Tian PF et al. Size-dependent capacitance study on InGaN-based micro-light-emitting diodes. *J Appl Phys* **116**, 044512 (2014).
82. Tang ZK, Jiang QM, Lu YY, Huang S, Yang S et al. 600-V normally off SiN_x/AlGaN/GaN MIS-HEMT with large gate swing and low current collapse. *IEEE Electron Device Lett* **34**, 1373–1375 (2013).
83. Wong MS, Hwang D, Alhassan AI, Lee C, Ley R et al. High efficiency of III-nitride micro-light-emitting diodes by sidewall passivation using atomic layer deposition. *Opt Express* **26**, 21324–21331 (2018).
84. Huang SC, Li H, Zhang ZH, Chen H, Wang SC et al. Superior characteristics of microscale light emitting diodes through tightly lateral oxide-confined scheme. *Appl Phys Lett* **110**, 021108 (2017).
85. Smith JM, Ley R, Wong MS, Baek YH, Kang JH et al. Comparison of size-dependent characteristics of blue and green InGaN microLEDs down to 1μm in diameter. *Appl Phys Lett* **116**, 071102 (2020).
86. Lin RZ, Jin ZX, Qiu PJ, Liao Y, Hoo J et al. High bandwidth series-biased green micro-LED array toward 6 Gbps visible light communication. *Opt Lett* **47**, 3343–3346 (2022).
87. Chang YH, Huang YM, Liou FJ, Chow CW, Liu Y et al. 2.805 Gbit/s high-bandwidth phosphor white light visible light communication utilizing an InGaN/GaN semipolar blue micro-LED. *Opt Express* **30**, 16938–16946 (2022).
88. Zhang Y, Wei ZX, Wang ZM, Fu HY. Real-time receive-forward NLOS visible light communication system based on multiple blue micro-LED nodes. *Photonics* **9**, 211 (2022).
89. Zhu SJ, Shan XY, Qiu PJ, Wang Z, Yuan ZX et al. Low-power high-bandwidth non-polar InGaN micro-LEDs at low current densities for energy-efficient visible light communication. *IEEE Photonics J* **14**, 7351805 (2022).
90. Xu FF, Jin ZX, Tao T, Tian PF, Wang GB et al. C-plane blue micro-LED with 1.53 GHz bandwidth for high-speed visible light communication. *IEEE Electron Device Lett* **43**, 910–913 (2022).
91. Wei ZX, Wang L, Liu ZX, Zhang C, Chen CJ et al. Multigigabit visible light communication based on high-bandwidth InGaN quantum dot green micro-LED. *ACS Photonics* **9**, 2354–2366 (2022).
92. Chang YH, Huang YM, Gunawan WH, Chang GH, Liou FJ et al. 4.343-Gbit/s green semipolar (20–21) μ-LED for high speed visible light communication. *IEEE Photonics J* **13**, 7300204 (2021).
93. Wang L, Wang L, Chen CJ, Chen KC, Hao ZB et al. Green InGaN quantum dots breaking through efficiency and bandwidth

bottlenecks of micro-LEDs. *Laser Photon. Rev* **15**, 2000406 (2021).
94. Lin RZ, Liu XY, Zhou GF, Qian ZY, Cui XG et al. InGaN micro-LED array enabled advanced underwater wireless optical communication and underwater charging. *Adv Opt Mater* **9**, 2002211 (2021).
95. Wang L, Wei ZX, Chen CJ, Wang L, Fu HY et al. 1.3 GHz E-O bandwidth GaN-based micro-LED for multi-gigabit visible light communication. *Photonics Res* **9**, 792–802 (2021).
96. Chen SWH, Huang YM, Chang YH, Lin Y, Liou FJ et al. High-bandwidth green semipolar (20 –21) InGaN/GaN micro light-emitting diodes for visible light communication. *ACS Photonics* **7**, 2228–2235 (2020).
97. Lan HY, Tseng IC, Kao HY, Lin YH, Lin GR et al. 752-MHz modulation bandwidth of high-speed blue micro light-emitting diodes. *IEEE J Quantum Electron* **54**, 3300106 (2018).
98. Ferreira RXG, Xie EY, McKendry JJD, Rajbhandari S, Chun H et al. High bandwidth GaN-based micro-LEDs for multi-Gb/s visible light communications. *IEEE Photonics Technol Lett* **28**, 2023–2026 (2016).
99. Ma ZH, Cao HC, Lin S, Li XD, Xi X et al. Optical and frequency degradation behavior of GaN-based micro-LEDs for visible light communication. *Opt Express* **28**, 12795–12804 (2020).
100. Cai YF, Haggar JIH, Zhu CQ, Feng P, Bai J et al. Direct epitaxial approach to achieve a monolithic on-chip integration of a HEMT and a single micro-LED with a high-modulation bandwidth. *ACS Appl Electron Mater* **3**, 445–450 (2021).
101. Zhao YJ, Fu HQ, Wang GT, Nakamura S. Toward ultimate efficiency: progress and prospects on planar and 3D nanostructured nonpolar and semipolar InGaN light-emitting diodes. *Adv Opt Photon* **10**, 246–308 (2018).
102. Rosales D, Gil B, Bretagnon T, Guizal B, Zhang F et al. Excitonic recombination dynamics in non-polar GaN/AlGaN quantum wells. *J Appl Phys* **115**, 073510 (2014).
103. Rashidi A, Monavarian M, Aragon A, Rishinaramangalam A, Feezell D. Nonpolar *m*-plane InGaN/GaN micro-scale light-emitting diode with 1.5 GHz modulation bandwidth. *IEEE Electron Device Lett* **39**, 520–523 (2018).
104. Johar MA, Song HG, Waseem A, Kang JH, Ha JS et al. Ultrafast carrier dynamics of conformally grown semi-polar $(11\bar{2}2)$ GaN/InGaN multiple quantum well co-axial nanowires on m-axial GaN core nanowires. *Nanoscale* **11**, 10932–10943 (2019).
105. Fu HQ, Lu ZJ, Zhao XH, Zhang YH, DenBaars SP et al. Study of low-efficiency droop in semipolar $(20\bar{2}1)$ InGaN light-emitting diodes by time-resolved photoluminescence. *J Disp Technol* **12**, 736–741 (2016).
106. Chen SWH, Shen CC, Wu TZ, Liao ZY, Chen LF et al. Full-color monolithic hybrid quantum dot nanoring micro light-emitting diodes with improved efficiency using atomic layer deposition and nonradiative resonant energy transfer. *Photonics Res* **7**, 416–422 (2019).
107. Haggar JIH, Ghataora SS, Trinito V, Bai J, Wang T. Study of the luminescence decay of a semipolar green light-emitting diode for visible light communications by time-resolved electroluminescence. *ACS Photonics* **9**, 2378–2384 (2022).
108. Choi HW, Liu C, Gu E, McConnell G, Girkin JM et al. GaN micro-light-emitting diode arrays with monolithically integrated sapphire microlenses. *Appl Phys Lett* **84**, 2253–2255 (2004).
109. Lin GR, Kuo HC, Cheng CH, Wu YC, Huang YM et al. Ultrafast 2x2 green micro-LED array for optical wireless communication beyond 5 Gbit/s. *Photonics Res* **9**, 2077–2087 (2021).
110. Zhang HJ, Li PP, Li HJ, Song J, Nakamura S et al. High polarization and fast modulation speed of dual wavelengths electroluminescence from semipolar (20 –21) micro light-emitting diodes with indium tin oxide surface grating. *Appl Phys Lett* **117**, 181105 (2020).
111. Gao HY, Yan FW, Zhang Y, Li JM, Zeng YP et al. Growth of nonpolar *a*-plane GaN on nano-patterned *r*-plane sapphire substrates. *Appl Surf Sci* **255**, 3664–3668 (2009).
112. Wang L, Wang L, Yu JD, Hao ZB, Luo Y et al. Abnormal stranski-krastanov mode growth of green InGaN quantum dots: morphology, optical properties, and applications in light-emitting devices. *ACS Appl Mater Interfaces* **11**, 1228–1238 (2019).
113. Arita M, Le Roux F, Holmes MJ, Kako S, Arakawa Y. Ultraclean single photon emission from a GaN quantum dot. *Nano Lett* **17**, 2902–2907 (2017).
114. Gačević Ž, Holmes M, Chernysheva E, Müeller M, Torres-Pardo A et al. Emission of linearly polarized single photons from quantum dots contained in nonpolar, semipolar, and polar sections of pencil-like InGaN/GaN nanowires. *ACS Photonics* **4**, 657–664 (2017).
115. Yang D, Wang L, Hao ZB, Luo Y, Sun CZ et al. Dislocation analysis of InGaN/GaN quantum dots grown by metal organic chemical vapor deposition. *Superlattices Microstruct* **99**, 221–225 (2016).
116. Lv WB, Wang L, Wang JX, Xing YC, Zheng JY et al. Green and red light-emitting diodes based on multilayer InGaN/GaN dots grown by growth interruption method. *Jpn J Appl Phys* **52**, 08JG13 (2013).
117. Lv WB, Wang L, Wang L, Xing YC, Yang D et al. InGaN quantum dot green light-emitting diodes with negligible blue shift of electroluminescence peak wavelength. *Appl Phys Express* **7**, 025203 (2014).
118. Wan RQ, Gao X, Wang LC, Zhang S, Chen XB et al. Phosphor-free single chip GaN-based white light emitting diodes with a moderate color rendering index and significantly enhanced communications bandwidth. *Photonics Res* **8**, 1110–1117 (2020).
119. Zhuang Z, Dai JP, Liu B, Guo X, Li Y et al. Improvement of color conversion and efficiency droop in hybrid light-emitting diodes utilizing an efficient non-radiative resonant energy transfer. *Appl Phys Lett* **109**, 141105 (2016).
120. Zhuang Z, Guo X, Liu B, Hu FR, Li Y et al. High color rendering index hybrid III-nitride/nanocrystals white light-emitting diodes. *Adv Funct Mater* **26**, 36–43 (2016).
121. Krishnan C, Brossard M, Lee KY, Huang JK, Lin CH et al. Hybrid photonic crystal light-emitting diode renders 123% color conversion effective quantum yield. *Optica* **3**, 503–509 (2016).
122. Wan RQ, Li GQ, Gao X, Liu ZQ, Li JH et al. Nanohole array structured GaN-based white LEDs with improved modulation bandwidth via plasmon resonance and non-radiative energy transfer. *Photonics Res* **9**, 1213–1217 (2021).
123. Rishinaramangalam AK, Ul Masabih SM, Fairchild MN, Wright JB, Shima DM et al. Controlled growth of ordered III-Nitride core-shell nanostructure arrays for visible optoelectronic devices. *J Electron Mater* **44**, 1255–1262 (2015).
124. Tzou AJ, Hsieh DH, Hong KB, Lin DW, Huang JK et al. High-

efficiency InGaN/GaN core-shell nanorod light-emitting diodes with low-peak blueshift and efficiency droop. *IEEE Trans Nanotechnol* **16**, 355–358 (2017).

125. Nami M, Rashidi A, Monavarian M, Mishkat-Ul-Masabih S, Rishinaramangalam AK et al. Electrically injected GHz-class GaN/InGaN core-nanowire-based μLEDs: carrier dynamics and nanoscale homogeneity. *ACS Photonics* **6**, 1618–1625 (2019).
126. Okamoto K, Niki I, Scherer A, Narukawa Y, Mukai T et al. Surface plasmon enhanced spontaneous emission rate of InGaN/GaN quantum wells probed by time-resolved photoluminescence spectroscopy. *Appl Phys Lett* **87**, 071102 (2005).
127. Gu XF, Qiu T, Zhang WJ, Chu PK. Light-emitting diodes enhanced by localized surface plasmon resonance. *Nanoscale Res Lett* **6**, 199 (2011).
128. Baets RG, Delbeke DG, Bockstaele R, Bienstman P. Resonant-cavity light-emitting diodes: a review. *Proc SPIE* **4996**, 74–86 (2003).
129. Ferrari L, Smalley JST, Qian HL, Tanaka A, Lu D et al. Design and analysis of blue InGaN/GaN plasmonic LED for high-speed, high-efficiency optical communications. *ACS Photonics* **5**, 3557–3564 (2018).
130. Xiao XT, Tang HD, Zhang TQ, Chen W, Chen WL et al. Improving the modulation bandwidth of LED by CdSe/ZnS quantum dots for visible light communication. *Opt Express* **24**, 21577–21586 (2016).
131. Laurand N, Guilhabert B, McKendry J, Kelly AE, Rae B et al. Colloidal quantum dot nanocomposites for visible wavelength conversion of modulated optical signals. *Opt Mater Express* **2**, 250–260 (2012).
132. Li HL, Chen XB, Guo JQ, Chen HD. A 550 Mbit/s real-time visible light communication system based on phosphorescent white light LED for practical high-speed low-complexity application. *Opt Express* **22**, 27203–27213 (2014).
133. Cho J, Park JH, Kim JK, Schubert EF. White light-emitting diodes: history, progress, and future. *Laser Photon Rev* **11**, 1600147 (2017).
134. Bulashevich KA, Karpov SY. Impact of surface recombination on efficiency of III-nitride light-emitting diodes. *Phys Status Solidi* (*RRL*)*-Rapid Res Lett* **10**, 480–484 (2016).
135. Hwang D, Mughal A, Pynn CD, Nakamura S, DenBaars SP. Sustained high external quantum efficiency in ultrasmall blue III-nitride micro-LEDs. *Appl Phys Express* **10**, 032101 (2017).
136. Le Minh H, O'Brien D, Faulkner G, Zeng LB, Lee K et al. 100-Mb/s NRZ visible light communications using a postequalized white LED. *IEEE Photonics Technol Lett* **21**, 1063–1065 (2009).
137. Hsu CW, Chen GH, Wei LY, Chow CW, Lu IC et al. Adaptive filtering for white-light LED visible light communication. *Opt Eng* **56**, 016115 (2017).
138. Hsu CW, Chow CW, Lu IC, Liu YL, Yeh CH et al. High speed imaging 3 x 3 MIMO phosphor white-light LED based visible light communication system. *IEEE Photonics J* **8**, 7907406 (2016).
139. Wu TZ, Lin Y, Huang YM, Liu M, Singh KJ et al. Highly stable full-color display device with VLC application potential using semipolar μLEDs and all-inorganic encapsulated perovskite nanocrystal. *Photonics Res* **9**, 2132–2143 (2021).
140. Huang HM, Wu HC, Huang C, Chen ZL, Wang C et al. Characteristics of micro-size light-emitting diode for illumination and visible light communication. *Phys Status Solidi* **215**, 1800484 (2018).
141. Xu YW, Chen J, Zhang H, Wei H, Zhou LJ et al. White-light-emitting flexible display devices based on double network hydrogels crosslinked by YAG: Ce phosphors. *J Mater Chem C* **8**, 247–252 (2020).
142. Li PP, Lu Y, Duan YM, Xu SQ, Zhang JJ. Potential application of perovskite glass material in photocatalysis field. *J Phys Chem C* **125**, 2382–2392 (2021).
143. Lin H, Wang B, Xu J, Zhang R, Chen H et al. Phosphor-in-glass for high-powered remote-type white AC-LED. *ACS Appl Mater Interfaces* **6**, 21264–21269 (2014).
144. Huang YM, Singh KJ, Hsieh TH, Langpoklakpam C, Lee TY et al. Gateway towards recent developments in quantum dot-based light-emitting diodes. *Nanoscale* **14**, 4042–4064 (2022).
145. Sapsford KE, Pons T, Medintz IL, Mattoussi H. Biosensing with luminescent semiconductor quantum dots. *Sensors* **6**, 925–953 (2006).
146. Chen SWH, Huang YM, Singh KJ, Hsu YC, Liou FY et al. Full-color micro-LED display with high color stability using semi-polar (20 –21) InGaN LEDs and quantum-dot photoresist. *Photonics Res* **8**, 630–636 (2020).
147. Yang X, Lin Y, Wu TZ, Yan ZJ, Chen Z et al. An overview on the principle of inkjet printing technique and its application in micro-display for augmented/virtual realities. *Opto-Electron Adv* **5**, 210123 (2022).
148. Alivisatos P. The use of nanocrystals in biological detection. *Nat Biotechnol* **22**, 47–52 (2004).
149. Ruan C, Zhang Y, Lu M, Ji CY, Sun C et al. White light-emitting diodes based on $AgInS_2$/ZnS quantum dots with improved bandwidth in visible light communication. *Nanomaterials* **6**, 13 (2016).
150. Cao HC, Lin S, Ma ZH, Li XD, Li J et al. Color converted white light-emitting diodes with 637.6 MHz modulation bandwidth. *IEEE Electron Device Lett* **40**, 267–270 (2019).
151. Protesescu L, Yakunin S, Bodnarchuk MI, Krieg F, Caputo R et al. Nanocrystals of cesium lead halide perovskites ($CsPbX_3$, X = Cl, Br, and I): novel optoelectronic materials showing bright emission with wide color gamut. *Nano Lett* **15**, 3692–3696 (2015).
152. Mei SL, Liu XY, Zhang WL, Liu R, Zheng LR et al. High-bandwidth white-light system combining a micro-LED with perovskite quantum dots for visible light communication. *ACS Appl Mater Interfaces* **10**, 5641–5648 (2018).
153. Singh KJ, Fan XT, Sadhu AS, Lin CH, Liou FJ et al. $CsPbBr_3$ perovskite quantum-dot paper exhibiting a highest 3 dB bandwidth and realizing a flexible white-light system for visible-light communication. *Photonics Res* **9**, 2341–2350 (2021).
154. Wang ZM, Wei ZX, Cai YT, Wang L, Li MT et al. Encapsulation-enabled perovskite-PMMA films combining a micro-LED for high-speed white-light communication. *ACS Appl Mater Interfaces* **13**, 54143–54151 (2021).
155. Soheyli E, Ghaemi B, Sahraei R, Sabzevari Z, Kharrazi S et al. Colloidal synthesis of tunably luminescent AgInS-based/ZnS core/shell quantum dots as biocompatible nano-probe for high-contrast fluorescence bioimaging. *Mater. Sci. Eng. C* **111**, 110807 (2020).
156. Li HJ, Li PP, Kang JJ, Li Z, Li ZC et al. Phosphor-free, color-tunable monolithic InGaN light-emitting diodes. *Appl Phys Express* **6**, 102103 (2013).

157. Lim SH, Ko YH, Rodriguez C, Gong SH, Cho YH. Electrically driven, phosphor-free, white light-emitting diodes using gallium nitride-based double concentric truncated pyramid structures. *Light Sci Appl* **5**, e16030 (2016).
158. Khoury M, Li HJ, Li PP, Chow YC, Bonef B et al. Polarized monolithic white semipolar (20 –21) InGaN light-emitting diodes grown on high quality (20 –21) GaN/sapphire templates and its application to visible light communication. *Nano Energy* **67**, 104236 (2020).
159. Chung RB, Lin YD, Koslow I, Pfaff N, Ohta H et al. Electroluminescence characterization of (2021) InGaN/GaN light emitting diodes with various wavelengths. *Jpn J Appl Phys* **49**, 070203 (2010).
160. Kowsz SJ, Young EC, Yonkee BP, Pynn CD, Farrell RM et al. Using tunnel junctions to grow monolithically integrated optically pumped semipolar III-nitride yellow quantum wells on top of electrically injected blue quantum wells. *Opt Express* **25**, 3841–3849 (2017).
161. Li HJ, Li PP, Zhang HJ, Chow YC, Wong MS et al. Electrically driven, polarized, phosphor-free white semipolar (20 –21) InGaN light-emitting diodes grown on semipolar bulk GaN substrate. *Opt Express* **28**, 13569–13575 (2020).
162. Haggar JIH, Cai YF, Bai J, Ghataora S, Wang T. Long-wavelength semipolar (11 –22) InGaN/GaN LEDs with Multi-Gb/s data transmission rates for VLC. *ACS Appl Electron Mater* **3**, 4236–4242 (2021).
163. Chun H, Rajbhandari S, Faulkner G, Tsonev D, Haas H et al. Demonstration of a Bi-directional visible light communication with an overall sum-rate of 110 Mb/s using LEDs as Emitter and Detector. In *Proceedings of 2014 IEEE Photonics Conference* 132–133 (IEEE, 2014); http://doi.org/10.1109/IPCon.2014.6995247
164. Stepniak G, Kowalczyk M, Maksymiuk L, Siuzdak J. Transmission beyond 100 Mbit/s using LED both as a transmitter and receiver. *IEEE Photonics Technol Lett* **27**, 2067–2070 (2015).
165. Liu XY, Lin RZ, Chen HL, Zhang SL, Qian ZY et al. High-bandwidth InGaN self-powered detector arrays toward MIMO visible light communication based on micro-LED arrays. *ACS Photonics* **6**, 3186–3195 (2019).
166. Chang YH, Hsu TC, Liou FJ, Chow CW, Liu Y et al. High-bandwidth InGaN/GaN semipolar micro-LED acting as a fast photodetector for visible light communications. *Opt Express* **29**, 37245–37252 (2021).
167. Chowdhury MZ, Shahjalal M, Hasan MK, Jang YM. The role of optical wireless communication technologies in 5G/6G and IoT solutions: prospects, directions, and challenges. *Appl Sci* **9**, 4367 (2019).
168. Zhang ZQ, Xiao Y, Ma Z, Xiao M, Ding ZG et al. 6G wireless networks: vision, requirements, architecture, and key technologies. *IEEE Veh Technol Mag* **14**, 28–41 (2019).
169. Yuan YF, Zhao YJ, Zong BQ, Parolari S. Potential key technologies for 6G mobile communications. *Sci China Inf Sci* **63**, 183301 (2020).
170. Sozer EM, Stojanovic M, Proakis JG. Underwater acoustic networks. *IEEE J Ocean Eng* **25**, 72–83 (2000).
171. Che XH, Wells I, Dickers G, Kear P, Gong XC. Re-evaluation of RF electromagnetic communication in underwater sensor networks. *IEEE Commun Mag* **48**, 143–151 (2010).
172. Zhu SJ, Chen XW, Liu XY, Zhang GQ, Tian PF. Recent progress in and perspectives of underwater wireless optical communication. *Prog Quantum Electron* **73**, 100274 (2020).
173. Chi N, Zhou YJ, Wei YR, Hu FC. Visible light communication in 6G: advances, challenges, and prospects. *IEEE Veh Technol Mag* **15**, 93–102 (2020).
174. Fan ZY, Lin JY, Jiang HX. III-nitride micro-emitter arrays: development and applications. *J Phys D Appl Phys* **41**, 094001 (2008).
175. Wei ZX, Zhang L, Wang L, Chen CJ, Pepe A et al. 2 Gbps/3 m air-underwater optical wireless communication based on a single-layer quantum dot blue micro-LED. *Opt Lett* **45**, 2616–2619 (2020).
176. Kim TK, Islam ABMH, Cha YJ, Kwak JS. 32 x 32 pixelated high-power flip-chip blue micro-LED-on-HFET arrays for submarine optical communication. *Nanomaterials* **11**, 3045 (2021).
177. Lu XY, Wang KH, Qiao L, Zhou W, Wang YG et al. Nonlinear compensation of multi-CAP VLC system employing clustering algorithm based perception decision. *IEEE Photonics J* **9**, 7906509 (2017).
178. Wen H, Luo KP, Chen QH, Geng K, Chen M et al. A novel sampling frequency offset mitigation scheme based on rotated K-means clustering for OFDM-VLC system. *Opt Commun* **513**, 128103 (2022).
179. Chi N, Zhao YH, Shi M, Zou P, Lu XY. Gaussian kernel-aided deep neural network equalizer utilized in underwater PAM8 visible light communication system. *Opt Express* **26**, 26700–26712 (2018).
180. Chen H, Jia JL, Niu WQ, Zhao YH, Chi N. Hybrid frequency domain aided temporal convolutional neural network with low network complexity utilized in UVLC system. *Opt Express* **29**, 3296–3308 (2021).
181. Ye H, Li GY, Juang BH. Power of deep learning for channel estimation and signal detection in OFDM systems. *IEEE Wirel Commun Lett* **7**, 114–117 (2018).
182. Farsad N, Goldsmith A. Neural network detection of data sequences in communication systems. *IEEE Trans Signal Process* **66**, 5663–5678 (2018).
183. Haigh PA, Ghassemlooy Z, Le Minh H, Rajbhandari S, Arca F et al. Exploiting equalization techniques for improving data rates in organic optoelectronic devices for visible light communications. *J Lightwave Technol* **30**, 3081–3088 (2012).
184. Wei ZX, Liu ZX, Liu X, Wang L, Wang L et al. 8.75 Gbps visible light communication link using an artificial neural network equalizer and a single-pixel blue micro-LED. *Opt Lett* **46**, 4670–4673 (2021).

Acknowledgements

We appreciate Prof. Rong Zhang and Prof. Minghui Hong from Xiamen University for the helpful discussion. We are grateful for the financial support from the National Natural Science Foundation of China (62274138, 11904302), Science and Technology Plan Project in Fujian Province of China (2021H0011), Fujian Province Central Guidance Local Science and Technology Development Fund Project in 2022 (2022L3058), Major Science and Technology Project of Xiamen, China (3502Z20191015) , and Foshan Hi-tech Zone High-tech Industrialization Entrepreneurial Team Special Guidance Fund in 2022 (222019000131).

Competing interests

The authors declare no competing financial interests.